

1        **Fast detection of tectonometamorphic discontinuities within the**  
2        **Himalayan orogen: structural and petrological constraints from**  
3                **Rasuwa District, Central Nepal Himalaya**

4

5

6        **GIULIA RAPA<sup>1</sup> , PIETRO MOSCA<sup>2</sup> , CHIARA GROPPPO<sup>1,2</sup> , FRANCO ROLFO<sup>1,2</sup>**

7        <sup>1</sup>Department of Earth Sciences, University of Torino, Via Valperga Caluso 35, 10125 Turin, Italy

8        (corresponding author: giulia.rapa@unito.it)

9        <sup>2</sup>Institute of Geosciences and Earth Resources - National Research Council of Italy (CNR), Via

10       Valperga Caluso 35, 10125 Turin, Italy

11

12 **Abstract**

13 A detailed structural, lithological and petrological study of different transects in the  
14 Rasuwa district of central Nepal Himalaya allows the characterization of the  
15 tectonostratigraphic architecture of the area. It also facilitates constraining the P-T  
16 evolution of the different units within the Lesser (LHS) and Greater (GHS) Himalayan  
17 Sequences. Peak  $P-T$  conditions obtained for the studied metapelite samples using  
18 the pseudosection approach and the Average PT method highlight the existence of  
19 four different  $T/P$  ratio populations in different tectonometamorphic units:  $80 \pm 11$   
20  $^{\circ}\text{C}/\text{kbar}$  (LHS),  $66 \pm 7$   $^{\circ}\text{C}/\text{kbar}$  (Ramgarh Thrust Sheet: LHS-Ramgarh Thrust Sheet),  
21  $73 \pm 1$   $^{\circ}\text{C}/\text{kbar}$  (Lower-GHS) and  $101 \pm 12$   $^{\circ}\text{C}/\text{kbar}$  (Upper-GHS). Integration of  
22 structural and petrological data emphasizes the existence of three  
23 tectonometamorphic discontinuities bounding these units, characterized by top-to-  
24 the-south sense of shear: the Ramgarh Thrust, which separates the LHS (peak  
25 metamorphism at  $\sim 600$   $^{\circ}\text{C}$ , 7.5 kbar) from the overlying LHS-Ramgarh Thrust Sheet  
26 (peak metamorphism at  $\sim 635$   $^{\circ}\text{C}$ , 10 kbar); the Main Central Thrust, which separates  
27 the LHS-Ramgarh Thrust Sheet from the Lower-GHS (peak at 700-740  $^{\circ}\text{C}$ , 9.5-10.5  
28 kbar with a prograde increase in both P and T in the kyanite stability field), and the  
29 Langtang Thrust, which juxtaposes the Upper-GHS (peak at 780-800 $^{\circ}\text{C}$ , 7.5-8.0 kbar  
30 with a nearly isobaric heating in the sillimanite stability field) onto the Lower-GHS. An  
31 increase in the intensity of deformation, with development of pervasive mylonitic  
32 fabrics and/or shear zones, is generally observed approaching the discontinuities  
33 from either side.

34 Overall, data and results presented in this paper demonstrate that petrological and  
35 structural analysis combined together, are reliable methods adequate to rapidly

36 identify tectonometamorphic discontinuities in both the LHS and GHS.  
37 Geochronological data from the literature allow the interpretation of these  
38 discontinuities as in-sequence thrusts.

39

40 **Keywords**

41 Himalaya; pseudosection; AvPT method; structural data; tectonometamorphic  
42 discontinuity.

43

## 44 **1. INTRODUCTION**

45 In the last few years, discoveries of tectonometamorphic discontinuities within the  
46 exhumed metamorphic core of the Himalayas (e.g. Larson et al., 2015; Montomoli et  
47 al., 2015 and references therein) marked the beginning of a new exciting frontier of  
48 research devoted to the understanding of the internal structure of the Himalayan  
49 orogen. These discontinuities, mostly interpreted as in-sequence thrusts, especially  
50 in western-central Nepal, separate rock packages characterized by different  
51 lithological associations, different geochemical features (e.g. Nd isotopes), different  
52 metamorphic evolutions and/or different peak metamorphic ages. Over the years,  
53 different criteria have been used to identify such discontinuities, including lithological  
54 (e.g. Gansser, 1983; Daniel et al. 2003), structural (e.g. Macfarlane et al., 1992;  
55 Reddy et al., 1993; Takagi et al., 2003; Law et al., 2004; Martin et al. 2005; Jessup et  
56 al., 2006; Searle et al., 2008; Yakymchuk and Godin, 2012; Larson et al. 2013;  
57 Larson and Cottle, 2014), geochemical (e.g. Robinson et al. 2001; Martin et al. 2005;  
58 Richards et al. 2005), petrological (e.g. Macfarlane, 1995; Fraser et al., 2000; Kohn  
59 et al., 2004; Goscombe et al., 2006; Kohn, 2008; Groppo et al., 2009; Imayama et al.,  
60 2010; Mosca et al., 2012; Yakymchuk and Godin, 2012; Larson et al. 2013; Wang et  
61 al., 2013, 2016; Rolfo et al., 2015; Rapa et al., 2016; Iaccarino et al., 2017) and  
62 geochronological (e.g. Harrison et al. 1997; Catlos et al. 2001, 2002; Kohn et al.,  
63 2004, 2005; Carosi et al., 2007, 2010; Kohn, 2008; Imayama et al., 2012; Larson et  
64 al. 2013; Montomoli et al., 2013; Rubatto et al., 2013; Larson and Cottle, 2014;  
65 Ambrose et al., 2015; Iaccarino et al., 2016) criteria.

66 The Rasuwa District of central Nepal Himalaya is an ideal natural laboratory for  
67 investigating the internal structure of both the Lesser Himalayan Sequence (LHS)

68 and Greater Himalayan Sequence (GHS) (Fig. 1). Because it offers both a complete  
69 cross-section through the LHS and GHS, and is easily accessible, different portions  
70 of this region have been investigated in detail since the '90s (e.g. Inger and Harris,  
71 1992; Macfarlane et al., 1992; Macfarlane, 1993, 1995; Upreti, 1999; Fraser et al.,  
72 2000; Kohn et al., 2004, 2005; Pearson and DeCelles, 2005; Kohn, 2008). It is not by  
73 chance that the first discontinuity within the GHS was identified in this region (Inger  
74 and Harris, 1992). In the following decades, other authors focused their attention on  
75 the Langtang region and recognized a number of major tectonometamorphic  
76 discontinuities within the GHS, using either petrological (e.g. Macfarlane, 1995;  
77 Fraser et al., 2000) or structural (Macfarlane et al., 1992; Reddy et al., 1993)  
78 evidences. More recently, Kohn et al. (2004, 2005) and Kohn (2004, 2008) combined  
79 P–T estimates with geochronological data, to infer the existence of major structures  
80 within the GHS (Langtang Thrust) and the LHS (Ramgarh Thrust or Munsiri Thrust),  
81 which separate the GHS and LHS in two sub-units, characterized by different peak  
82 P–T conditions and by different P–T–t paths.

83 Although the tectonometamorphic architecture of Langtang is relatively well-known, a  
84 combined structural and petrological study of both the LHS and GHS in this region is  
85 lacking. Moreover, most of the petrological studies published so far on the Langtang  
86 transect, constrained the peak P-T conditions experienced by the different LHS and  
87 GHS units, but did not provide information about their P-T paths or evolution. This  
88 study aims to fill this knowledge gap. We present new detailed structural, lithological  
89 and petrological data for the Langtang transect and for the adjacent western sector  
90 towards the village of Gatlang (Fig. 2). These new data, combined with those already  
91 published by Rapa et al. (2016) for the nearby Gosainkund-Helambu region, allow us

92 to fully characterize the tectonostratigraphic architecture of the area, and to constrain  
93 the P-T evolution of the different units within the LHS and the GHS.

94

## 95 **2. GEOLOGICAL SETTING**

96 The Himalayan orogen derives from the continued collision of the Indian and  
97 Eurasian plates, which began at ca. 50 Ma. Its present structure is characterized by  
98 four tectonostratigraphic units that extend longitudinally for more than 2000km and  
99 are bounded by crustal-scale north-dipping faults (Fig 1).

100 The uppermost unit is the Tethyan Sedimentary Sequence (TSS: e.g. Gaetani and  
101 Garzanti, 1991), separated from the subjacent Greater Himalayan Sequence (GHS)  
102 by the South Tibetan Detachment System (STDS).

103 The Greater Himalayan Sequence (GHS) represents the exhumed metamorphic core  
104 of the Himalaya and consists of several km thick sequence of medium-grade to  
105 anatectic rocks bounded at its top by the STDS and at its base by the Main Central  
106 Thrust (MCT). At least two main domains can be broadly identified within the GHS,  
107 characterized by rocks which experienced different metamorphic evolutions (i.e.  
108 different P-T paths: e.g. Larson et al., 2010; Mosca et al., 2012; Montomoli et al.,  
109 2015 and references therein; Rapa et al., 2016). The lower structural levels of the  
110 GHS (Lower-GHS) are medium- to high grade metasediments and granitic  
111 orthogneisses, recording a metamorphic grade that increases structurally upward  
112 from the garnet and staurolite zones to the sillimanite zone and, locally, to anatexis  
113 (e.g. Goscombe et al., 2006; Groppo et al., 2009, 2010; Mosca et al., 2012). The  
114 upper GHS (Upper-GHS), roughly corresponds to the Higher Himalayan Crystallines  
115 (Pognante and Benna, 1993; Lombardo et al., 1993) and consists of high-grade,  
116 often migmatitic, para- and orthogneisses. The Upper-GHS rocks often host dyke

117 networks and lens-shaped bodies of two-mica and tourmaline-bearing leucogranites,  
118 characterized by a progressive decrease in peak-pressure structurally up section  
119 (Lombardo et al., 1993; Pognante and Benna, 1993; Davidson et al., 1997; Guillot,  
120 1999; Hodges, 2000; Groppo et al., 2012, 2013).

121 The underlying Lesser Himalayan Sequence (LHS) consists of low-grade  
122 metasediments (metapelitic schists, impure marbles, calcschists and quartzites)  
123 associated with granitic orthogneiss. To the south, the LHS lithologies are juxtaposed  
124 with the molassic sediments of the Siwalik foreland across the Main Boundary Thrust  
125 (MBT, Fig. 1). Numerous stratigraphic classifications have been proposed for the  
126 LHS across the Himalaya, and correlations through different regions are not  
127 straightforward (e.g. Upreti, 1999; McQuarrie et al., 2008, Kohn et al., 2010 and  
128 references therein).

129 In the Gatlang-Langtang and Gosainkund-Helambu regions investigated in this study  
130 (Fig. 1), the main tectonic structures bounding these units are the Ramgarh Thrust,  
131 the Main Central Thrust and the Langtang Thrust. The Main Central Thrust (MCT)  
132 was one of the first crustal-scale tectonic discontinuities described in the Himalaya.  
133 This is a large thrust-sense shear zone (MCTZ, Main Central Thrust Zone), ranging in  
134 thickness from several hundreds of metres to several kilometres, which emplaces the  
135 medium- to high-grade Lower-GHS over the low-grade LHS. The MCT has been  
136 mapped across the Himalaya using a variety of different criteria (see Searle et al.,  
137 2008 and Martin, 2017 for a review), and despite being the subject of numerous  
138 studies over the last few decades, it remains one of the most debated tectonic  
139 features of the Himalaya. In central Nepal movement along it has been dated at 24-  
140 18 Ma (Godin et al., 2006 for a review). In the Gatlang-Langtang and Gosainkund-  
141 Helambu areas, the MCTZ was first mapped by Arita et al. (1973) as a structural

142 discordance at the base of the GHS anatectic rocks. McFarlane (1992) located the  
143 MCTZ between the LHS (mainly pelitic and graphitic schists of the Dunche schists  
144 formation) and the GHS (Gosaikunda anatectic gneiss), and she described it as an  
145 imbricate shear zone consisting of different lithological units of both LHS and GHS  
146 affinity, separated by brittle faults. Later on, Takagi et al. (2003) subdivided the  
147 MCTZ into three units involving lithologies from the upper LHS and the lower part of  
148 GHS, and emphasized the occurrence of a late top-to-the-north extensional  
149 movement along the MCTZ itself.

150 The Ramgarh Thrust was first identified in the Langtang region by Pearson and  
151 DeCelles (2005), combining stratigraphic relationships and Nd isotopic analysis. The  
152 Ramgarh Thrust is a discrete tectonostratigraphic boundary located within the LHS  
153 (i.e. below the MCTZ), and places the Robang Formation (~1940 Ma according to  
154 Pearson & DeCelles, 2005), including also Lower Proterozoic augen gneisses (Ulleri  
155 gneiss) and quartzites, above the younger Kuncha Formation (~1860 Ma; e.g.  
156 Schelling, 1992; DeCelles et al., 2001; Robinson et al., 2001; Pearson, 2002;  
157 Pearson & DeCelles, 2005).

158 The Langtang Thrust was first identified in the Langtang region by Kohn et al. (2004,  
159 2005) basing on metamorphic and geochronological criteria, although prior to these  
160 studies, other authors already described the existence of a major discontinuity within  
161 the GHS in the region (Inger and Harris, 1992; Macfarlane, 1995; Fraser et al., 2000).  
162 The Langtang Thrust is mainly a metamorphic discontinuity that separates a lower  
163 GHS unit (Lower-GHS), characterized by higher pressure at peak-T conditions, from  
164 an upper GHS unit (Upper-GHS), which experienced lower pressure at peak-T  
165 conditions (e.g. Kohn, 2008).

166



167 **3. METHODS**

168 **3.1 Fieldwork**

169 A detailed geological study combined with mesostructural observations was  
170 conducted in central Nepal Himalaya along three transects, crossing both the LHS  
171 and the GHS exposed in the Gatlang, Langtang and Gosainkund-Helambu regions  
172 (Fig. 1 and 2). A geological map as well as stereo plots of structural elements are  
173 shown in Fig. 2. Representative photos of lithologies and meso-structures are given  
174 in Figs. 3-7.

175

176 **3.2 Petrography and mineral chemistry**

177 A total of 184 thin sections were petrographically characterized. Detailed petrologic  
178 study was performed on a total of 14 metapelite samples: five from the Gatlang  
179 transect (samples 15-19, 14-27a, 15-28b, 15-26b and 15-38), five from the Langtang  
180 transect (samples 14-03, 14-25b, 14-24, 14-08a and 14-12) and four from the  
181 Gosainkund-Helambu transect (samples 14-44a, 14-61b, 14-71 and 14-52). Nine of  
182 these samples have been already described and petrologically modelled using the  
183 pseudosection approach by Rapa et al. (2016). Those samples are not described in  
184 detail in Section 4.2, but their microstructures are relevant to this study and are  
185 summarized in Table 1. Petrographic and mineral chemical features are described in  
186 detail for samples 15-19, 15-28b, 15-26b, 15-38 and 14-12.

187 The rock-forming minerals were analyzed with either a Cambridge Stereoscan 360  
188 (analyses performed prior to 2016) or a Jeol JSM-IT300LV (analyses performed  
189 since 2016) Scanning Electron Microscope at the Department of Earth Sciences,  
190 University of Torino. Both the instruments were equipped with an energy dispersive  
191 spectrometry (EDS) Energy 200 system and an SDD X-Act3 detector (Oxford Inca

192 Energy). The operating conditions were 50 s counting time and 15 kV accelerating  
193 voltage. SEM-EDS quantitative data (spot size 2  $\mu\text{m}$ ) were acquired and processed  
194 using the Microanalysis Suite Issue 12, INCA Suite version 4.01; natural mineral  
195 standards were used to calibrate the raw data; the  $\phi\rho Z$  correction (Pouchou and  
196 Pichoir, 1988) was applied. Table 2 summarizes the representative chemical  
197 compositions for the main minerals in each sample. Mineral abbreviations are  
198 according to Whitney and Evans (2010). **Representative photos of microstructures**  
199 **are presented in Fig. 8.**

200

### 201 **3.3 Optimal thermobarometry**

202 The Thermocalc “Average PT” (AvPT) method (i.e. “Optimal thermobarometry”:  
203 Powell and Holland, 1994) was applied to all of the samples in this study including  
204 the 9 samples already investigated using the P-T pseudosection approach by Rapa  
205 et al., (2016). Thermocalc v3.33 (Powell and Holland, 1994) and the Holland and  
206 Powell (1998, revised in 2004) dataset were used. Activity-composition relationships  
207 were calculated using the software AX. The internal consistency of the method was  
208 examined with the samples additionally investigated using the pseudosection  
209 approach (both in this paper and in Rapa et al., 2016). To maintain the consistency  
210 between the thermodynamic datasets used for pseudosections and AvPT, we chose  
211 not to use the updated version of the dataset (version 6.02) based on Holland and  
212 Powell (2011).

213 The AvPT method evaluates P-T conditions through the calculation of a set of  
214 independent reactions representing all the equilibria between the end-members of  
215 the equilibrium assemblage; if the number of reactions between end-members is too  
216 low, the method does not converge to a result. Mineral compositions used for

217 thermobarometric calculations are given in Tables S1a-e, and results in Table 3. For  
218 samples with zoned garnets, calculations were done considering garnet core and  
219 garnet rim compositions, combined with the mineral assemblages in equilibrium with  
220 each of them. The presence of melt in equilibrium with the peak mineral assemblage  
221 in some samples was simulated by reducing the activity of H<sub>2</sub>O ( $0.7 < a_{\text{H}_2\text{O}} < 1$ ) (see  
222 Mosca et al., 2012), because it is not possible to include the melt solution model in  
223 AvPT calculations.

224

### 225 **3.4 Pseudosection modelling**

226 One sample (15-26b) out of the 14 samples investigated in this study has been  
227 modelled using the pseudosection approach in the system MnNCKFMASH; Fe<sup>3+</sup>  
228 was neglected because Fe<sup>3+</sup>-rich oxides are absent and the amount of Fe<sup>3+</sup> in the  
229 analyzed minerals is very low. Pseudosections for nine additional samples have been  
230 already calculated and discussed in detail by Rapa et al. (2016).

231 Pseudosections were calculated using Perplex 6.7.2 (version June 2015; Connolly,  
232 1990, 2009) and the internally consistent thermodynamic dataset and equation of  
233 state for H<sub>2</sub>O of Holland and Powell (1998, revised 2004). The minerals considered in  
234 the calculation were: garnet, biotite, chlorite, kyanite, andalusite, sillimanite,  
235 staurolite, zoisite/clinozoisite, plagioclase, white mica, K-feldspar, cordierite, quartz,  
236 titanite, rutile, ilmenite, in addition to melt. The following solution models were used:  
237 garnet, chloritoid, cordierite and staurolite (Holland and Powell, 1998), biotite  
238 (Tajčmanová et al., 2009), chlorite (Holland et al., 1998), plagioclase (Newton et al.,  
239 1980), white mica (Coggon and Holland 2002; Auzanneau et al., 2010), K-feldspar  
240 (Thompson and Hovis, 1979), and melt (Holland and Powell, 2001; White et al.,  
241 2001, 2007). The fluid was considered as pure H<sub>2</sub>O ( $a_{\text{H}_2\text{O}}=1$ ).

242

## 243 **4. RESULTS**

244

### 245 **4.1 Tectonostratigraphy of the Gatlang, Langtang, and Gosainkund-Helambu** 246 **regions**

247 Along the Gatlang, Langtang and Gosainkund-Helambu transects, both the LHS and  
248 the GHS tectonostratigraphic units are exposed, the latter being subdivided into the  
249 Lower-GHS and the Upper-GHS.

250

#### 251 **4.1.1 Lesser Himalayan Sequence**

##### 252 *Lithostratigraphic features*

253 The LHS is exposed in the westernmost part of the study area, south of the village of  
254 Syabrubensi, and it extends northward up to Tatopani (Fig. 2). In its structurally lower  
255 levels, the LHS is mainly composed of grey to pale-green, fine-grained phyllites,  
256 slates and phyllitic schists (Fig. 3a,b), with ubiquitous dm-thick intercalations of  
257 metasediments characterized by the occurrence of detrital grains of quartz, feldspar  
258 and tourmaline. The gradual increase of metamorphic grade up-section (i.e. from SW  
259 to NE) is already evident at the outcrop scale and is evidenced by the occurrence of  
260 Chl + Wm assemblages at the lowest structural levels, passing to two-mica ( $\pm$ Grt  $\pm$ St  
261  $\pm$ Ky) assemblages close to the MCT. In its uppermost structural levels, the LHS is  
262 more heterogeneous, with several carbonatic and graphitic units intercalated with the  
263 phyllites. Specifically, the most common lithologies include: (i) laminated impure  
264 marbles, calcareous phyllites and calcschists, and (ii) dm-thick layers of graphitic  
265 schists. The bedding in the marbles is mm- to pluri-cm thick, and the foliation is  
266 defined by the preferred orientation of Wm  $\pm$  Phl  $\pm$  Chl  $\pm$  Amph. Calcareous phyllites

267 and calcschists occur as dm-thick layers and contain Wm ± Bt ± Phl ± Chl ± Gr in  
268 varying proportions.

269 The dominantly phyllitic lithologies with quartzitic intercalations exposed at the  
270 lowermost structural levels of the LHS can be ascribed to the Lower-LHS according  
271 to the definition of Kohn et al. (2010) (also known as Kuncha and Ranimata  
272 Formations in central and western Nepal, respectively; Stöcklin, 1980; Person and  
273 DeCelles, 2005; Robinson et al., 2006); the abundant carbonatic and graphitic rocks  
274 can be ascribed to the Upper-LHS (Kohn et al., 2010).

275 Upward in the sequence, the dominantly carbonatic and graphitic lithologies give way  
276 to strongly foliated phyllitic schists with abundant intercalations of Wm ± Bt ± Chl ± St  
277 banded quartzite (Fig. 3c,d), and by two-mica mylonitic orthogneisses forming a  
278 decametric-thick body thinning towards SE (Fig. 3e,f). Pearson and DeCelles (2005)  
279 ascribed the quartzites and phyllitic schists to the Kushma and Robang Formations,  
280 respectively, which represent the lowermost Paleoproterozoic levels of the LHS. The  
281 mylonitic augen-gneiss may be correlated to the Ulleri gneiss (e.g. Le Fort and Rai,  
282 1999), stratigraphically intercalated within the lowermost portion of the Kuncha-  
283 Ranimata Formations in the Lower-LHS. This suggests that, in the study area, Lower-  
284 LHS lithologies (i.e. quartzites: Robang-Kushma Fm.; augen gneisses: Ulleri gneiss)  
285 are tectonically emplaced over Upper-LHS lithologies (i.e. calcschists and marbles).  
286 The thrust fault responsible for this emplacement, the Ramgarh Thrust, has been  
287 documented by a number of authors (e.g. Schelling, 1992; DeCelles et al., 2001;  
288 Robinson et al., 2001; Pearson, 2002; Kohn et al., 2004) basing on stratigraphic,  
289 geochemical (Nd isotopic analysis) and geochronological data. In the following, the  
290 relatively thin package of Lower-LHS lithologies bounded by the Ramgarh Thrust at

291 its bottom and by the MCT at its top, will be referred to as LHS-Ramgarh Thrust  
292 Sheet.

293

#### 294 *Structural features*

295 The main pervasive foliation in the LHS is represented by the  $S_{2(LHS)}$ , which resulted  
296 from a ductile  $D_{2(LHS)}$  deformation event intensively transposing earlier planar  
297 elements (i.e. bedding and an early  $S_{1(LHS)}$  foliation). At the outcrop scale, planar  
298 elements can, therefore, be generally described as a  $S_2$ - $S_{1(LHS)}$  composite foliation  
299 (Figs. 3a,e and Fig. 4a,b).

300 In the phyllites, the  $S_{2(LHS)}$  is defined by  $Wm \pm Chl \pm Bt$ ; the rim of porphyroblastic  
301 garnet is locally in equilibrium with this foliation. The  $S_{2(LHS)}$  transposed an early  
302  $S_{1(LHS)}$  foliation defined by  $Wm \pm Chl \pm Bt$ , locally preserved in microlithons as well as  
303 an internal foliation ( $Chl + Ilm \pm Gr$ ) in garnet porphyroblasts (Fig. 3b). Syntectonic  
304 quartz veins are often stretched and boudinated along the  $S_{2(LHS)}$ . In marbles, the  
305  $S_{2(LHS)}$  is roughly parallel to a mm- to cm- thick compositional bedding, and it is  
306 marked by the preferred orientation of  $Wm \pm Phl \pm Chl \pm Amph$ . In a few quartzite  
307 outcrops, the dominant  $S_{2(LHS)}$  is at high angle with respect to an original  
308 compositional banding. In the augen-gneisses, the  $S_{2(LHS)}$  manifests as a mylonitic  
309 foliation defined by  $Bt + Wm$  layers wrapping around rotated  $Kfs \pm Pl$  porphyroclasts  
310 (Fig. 3f). The aplites intercalated within the augen-gneisses are mostly transposed in  
311 the  $S_{2(LHS)}$  foliation.

312 The  $S_{2(LHS)}$  dips, on average, to the NNE in the northern sectors of the study area and  
313 progressively rotates towards NE-ENE moving to the east. It contains a  $L_{2(LHS)}$   
314 stretching lineation (defined by elongated  $Kfs$  porphyroclasts and minerals) plunging  
315 between N and NE.  $F_{2(LHS)}$  folds (whose axial plane is approximated by the  $S_{2(LHS)}$ )

316 have stretched limbs and slightly thickened hinges, and often have an asymmetric  
317 shape, synthetic with top-to-the-south shearing. The relationships between  $L_{2(LHS)}$  and  
318  $F_{2(LHS)}$  axes suggest non-cylindrical folding. The abundant kinematic indicators (e.g.  
319 mica-fish, rotated clasts, S-C shear cleavages, asymmetry of stretched Qz lenses) at  
320 outcrop and microscope scale indicate a consistent top-to-the-south-southwest sense  
321 of shear (Fig. 4a,b).  $S_{2(LHS)}$  and C-surfaces intersect on average between  $30^\circ$  and  
322  $10^\circ$ .

323 Mesoscopic shear zones (from cm- to metre-thick) related to the  $D_{2(LHS)}$  event can be  
324 identified in several outcrops, resulting either parallel with or at very low angle to the  
325  $S_{2(LHS)}$ . Field observations indicate that the abundance of these shear zones, marked  
326 by the pervasive occurrence of stretched folds and stretched veins of Qz, significantly  
327 increases around Syabrubensi (i.e. approaching the top of the LHS, and within the  
328 LHS-Ramgarh Thrust Sheet).

329 Structural features related to the  $D_{2(LHS)}$  are overprinted by a  $D_{3(LHS)}$  phase  
330 represented by a crenulation event and local development of open folds (Fig. 4c).  
331 The crenulation lineation  $L_{cr3(LHS)}$  plunges towards NE and E, resting on most of the  
332 outcrops at angle  $<40^\circ$  with respect to the  $L_{2(LHS)}$  (Fig. 4d). The crenulation cleavage  
333  $S_{3(LHS)}$  is mostly defined by Bt + Wm. A later  $D_{4(LHS)}$  phase is marked by N-S to NW-  
334 SE trending folds, usually open, with axes plunging at low/moderate angle to the N  
335 and NW and sub-vertical axial planes. In addition, locally aligned Bt, Wm and/or Chl  
336 flakes have been observed statically overgrowing the  $S_{2(LHS)}$  foliation.

337 Late top-to-the-north extension is recorded by shear band cleavages dipping to the  
338 north (Fig. 4e,f) at low angle with respect to the main foliation, and by local  
339 development of extension gashes, mainly observed in the Upper-LHS lithologies  
340 below the LHS-Ramgarh Thrust Sheet.

341

## 342 **4.1.2 Lower Greater Himalayan Sequence**

### 343 *Lithological features*

344 The Lower-GHS lithologies are characterized by highly variable grain size, which is  
345 generally coarser than that of the LHS lithologies. The most frequent lithology is a  
346 medium-grained two-mica gneissic micaschist with porphyroblastic dark-red Grt  $\pm$  Ky  
347  $\pm$  St (Fig. 5a). These rocks exhibit a compositional layering defined by Wm + Bt  
348 continuous domains alternating with discontinuous Qz + Pl domains; the main planar  
349 foliation is defined by Bt and Wm flakes (up to ~5 mm in length). Locally, a later  
350 generation of Wm statically overgrows the planar fabric (Fig. S1a). Ky occurs as large  
351 idioblasts, mainly oriented parallel to the main foliation or overgrowing it (Fig. 5**Error!**  
352 **Reference source not found.**b). St is rarely observed at the outcrop scale. Layers of  
353 fine-grained two-mica or Bt + Grt -bearing gneisses are often intercalated within  
354 these two-mica gneissic micaschists (Fig. 5c); their relative abundance is highly  
355 variable, and they range in thickness between few centimetres and several metres.

356 In the structurally higher levels of the Lower-GHS, fibrolitic Sil appears, especially  
357 along the Gosainkund-Helambu transect. The most common lithology at these  
358 structural levels is a two-mica + Grt  $\pm$  Sil micaschist or gneissic micaschist with a  
359 well-developed foliation defined by the preferred orientation of Bt, minor Wm  $\pm$  Sil  $\pm$   
360 Qz  $\pm$  Pl concentrated in continuous mm-thick layers, alternated with pluri-mm Qz + Pl  
361  $\pm$  Kfs  $\pm$  Bt leucocratic domains (Fig. S1b). Structurally upward in the sequence,  
362 microstructures indicating the presence of former melt appear, including leucosomic  
363 pods and symplectites related to back-reactions between solids and melt (e.g.  
364 Waters, 2001; Cenki *et al.*, 2002; Kriegsman and Alvarez-Valero, 2010) and



365 “pseudomorphs after melt” (according to the definition of Holness and Clemens,  
366 1999; Holness and Sawyer, 2008) (Fig. 5d).

367 Calc-silicate rocks occur in the Lower-GHS as dm-thick deformed layers or metre-  
368 sized massive boudins enveloped by the main schistosity (Fig. 5e). Calc-silicate  
369 rocks commonly consist of Grt + Cpx + Pl + Qz ( $\pm$  Zo  $\pm$  Amph  $\pm$  Cal), and have a  
370 granofelsic structure; a banded structure is observed locally. Layers of quartzites  
371 occur in the lowermost part of the Lower-GHS (Fig. 5f). These rocks are especially  
372 abundant along the Bothe Khosi River, where they constitute dm- to m- thick layers  
373 intercalated in the metapelites. The quartzites are pale-green to greyish and locally  
374 banded, with white mica and phlogopite defining the main foliation.

375 In the Gosainkund-Helambu region (Fig. 2), a pluri-km body of a two-mica  
376 orthogneiss is hosted within the Lower-GHS metapelites. The orthogneiss shows a  
377 well-developed schistosity and cm- to pluri-cm Qz + Fsp eyes, stretched parallel to  
378 the main foliation. Where deformation is less pervasive, the porphyric structure of the  
379 granitic protolith is still preserved.

380

### 381 *Structural features*

382 The two-mica + Grt  $\pm$  Ky  $\pm$  St gneisses and schists exposed at the lowermost  
383 structural levels of the Lower-GHS are intensively deformed and show a pervasive  
384 fabric defined by discontinuous Qz + Pl leucocratic domains alternating with dark to  
385 grey pluri-mm thick layers consisting of Wm + Bt + Grt  $\pm$  Ky  $\pm$  St (Fig. 5a). The  
386 compositional banding is often parallel to the main pervasive foliation, here referred  
387 to as  $S_{2(L-GHS)}$  and defined by Bt  $\pm$  Wm  $\pm$  Ky  $\pm$  St (Fig. 5a,c). The  $S_{2(L-GHS)}$  derives from  
388 the transposition of an earlier foliation  $S_{1(L-GHS)}$ . The  $S_{1(L-GHS)}$  is preserved in  
389 microlithons, intrafolial folds and isolated fold hinges. The  $S_{1(L-GHS)}$  can be observed

390 as a compositional banding in quartzites, where it is defined by Wm and Bt, and more  
391 rarely in fine-grained gneisses and micaschists. Grt porphyroblasts (up to 2 mm in  
392 diameter) are microstructurally in equilibrium with micas defining the  $S_{2(L-GHS)}$ . Ky  
393 blades, up to several mm in length, have been observed either randomly distributed  
394 on the  $S_{2(L-GHS)}$  surface or aligned to define a mineral lineation  $L_{2(L-GHS)}$ .

395 In the orthogneiss, the  $S_{2(L-GHS)}$  is defined by Bt + Wm alignment that envelops  
396 deformed K-feldspar and plagioclase porphyroclasts, often defining a pervasive  
397 lineation  $L_{2(L-GHS)}$ .

398 On average, the  $S_{2(L-GHS)}$  dips moderately towards NNE and E, dipping steeper in the  
399 middle part of the Bothe Khosi valley (Fig. 2). Along the southernmost part of the  
400 Helambu transect, the  $S_{2(L-GHS)}$  dips towards S. Biotite, white mica and locally  
401 sillimanite define a  $L_{2(L-GHS)}$  down-dip mineral lineation.

402 The  $S_{2(L-GHS)}$  is deformed by a  $D_{3(L-GHS)}$  folding event, associated with the  
403 development of a locally pervasive  $S_{3(L-GHS)}$  crenulation cleavage defined by Bt + Wm  
404 (Fig. 6a). The  $L_{cr3(L-GHS)}$  crenulation lineation and the  $F_{3(L-GHS)}$  fold axes (also  
405 identified by  $S_3$ - $S_{2(L-GHS)}$  intersection lineation) plunge moderately to steeply (up to  
406  $60^\circ$ ) to the NE and E. In highly deformed areas, the mesoscale  $F_{3(L-GHS)}$  folds are  
407 isoclinal to tight, and the  $S_{3(L-GHS)}$  is highly penetrative, transposing the  $S_{2(L-GHS)}$  (Fig.  
408 6b-d). There, localized shear zones are approximately parallel to the  $S_{3(L-GHS)}$ , and  
409 the  $F_{3(L-GHS)}$  folds show stretched limbs. Aligned biotite and locally kyanite define  
410 down-dip mineral lineations on the  $S_3$ - $S_{2(L-GHS)}$  composite foliation. Pinch-and-swell  
411 structures of syntectonic quartz veins and foliations related to  $D_{2(L-GHS)}$  and  $D_{3(L-GHS)}$   
412 events are present in several outcrops (Fig. 6). Kinematic indicators (e.g. S-C  
413 cleavage relationships, mica-fish, rotated clasts) indicate top-to-the-south sense of  
414 shear during both  $D_{2(L-GHS)}$  and  $D_{3(L-GHS)}$  deformation events.

415

### 416 **4.1.3 Upper Greater Himalayan Sequence**

#### 417 *Lithological features*

418 The most common lithology in the Upper-GHS is Grt + Kfs + Sil migmatitic  
419 paragneiss. At the outcrop scale, these rocks typically consist of mm- to cm- thick  
420 leucocratic quartz-feldspathic domains alternating with mm- thick dark Bt + Pl + Sil ±  
421 Grt layers, which generally define a more or less continuous planar foliation (Fig. 7a).  
422 The amount of garnet in the unit is variable. It occurs as mm- to cm-sized  
423 porphyroblasts that are often surrounded by a Pl corona (Fig. 7b and Fig. 8i). A late  
424 Wm generation locally occurs as large flakes overgrowing the main foliation.

425 Calc-silicate granofels and gneiss occur as tens of metre thick layers within the  
426 hosting metapelites (Fig. 7c). They are easily recognized in the field because of their  
427 characteristic deformation styles, due to their relatively weak rheological behaviour  
428 compared to the host Qz + Fsp -rich rocks. The main mineral assemblage consists of  
429 Cpx + Kfs + Scp ± Pl ± Qz ± Cal, with late green Amph. A banded structure is  
430 observed, defined by the different modal proportion of the rock-forming minerals in  
431 adjacent layers, possibly reflecting a primary compositional banding.

432 Large bodies of migmatitic Bt + Sil ± Grt orthogneiss, that are concordant with the  
433 regional foliation, are present at different structural levels. Metre- to tens of metre  
434 thick layers of fine-grained biotitic gneiss with Sil-rich nodules (“Black Gneisses”  
435 according to Lombardo et al., 1993) are sometimes associated with the orthogneiss  
436 (Fig. 7d). The nodules, up to several cm in length, mainly consist of Sil + Qz and are  
437 flattened parallel to the foliation. Pegmatitic dykes and two-mica + Grt + Tur  
438 leucogranite bodies and dykes occur at the higher structural levels of the Upper-  
439 GHS, and are variably oriented with respect to the main foliation. These

440 leucogranites are the dominant lithology in the highest peaks of the Langtang Valley  
441 (e.g. Langtang Lirung, Langtang II, Kimshung).

442

#### 443 *Structural features*

444 The various penetrative structures occurring in the high-grade, often migmatitic,  
445 Upper-GHS lithologies are difficult to be univocally interpreted at the mesoscale due  
446 to the interplay between melt-producing processes, melt-crystallizing processes and  
447 tectonic processes. Relicts of a foliation older than the main pervasive foliation have  
448 not been observed, perhaps reflecting complete transposition. It is therefore not  
449 possible to ascribe the main regional schistosity to a specific deformational phase,  
450 and to correlate it with the planar fabrics observed in the LHS and in the Lower-GHS  
451 units. In other words, it is not possible to understand if the main foliation is a  $S_{1(U-GHS)}$   
452 or a  $S_{2(U-GHS)}$ , therefore the neutral term  $S_{m(U-GHS)}$  (main schistosity) has been  
453 preferred.

454 The migmatites are characterized by a banded structure, defined by Bt + Sil + Qz ±  
455 Grt mm-thick mesocratic domains, alternating with Qz + Pl + Kfs ± Sil ± Grt pluri-mm  
456 leucocratic layers (Fig. 7a,e,f). The  $S_{m(U-GHS)}$  planar fabric is parallel to the  
457 compositional layering and is marked by the alignment of Bt and fibrolitic Sil.  
458 Leucosomes are almost parallel to the  $S_{m(U-GHS)}$  and contain a planar fabric defined  
459 by biotite, thus suggesting that melting was contemporary to the  $S_{m(U-GHS)}$   
460 development.

461 Calc-silicate rocks are either stretched and deformed (Fig. 7c), or, more rarely, form  
462 boudins enveloped by the  $S_{m(U-GHS)}$ , depending on their mineral assemblage. The  
463 migmatitic orthogneisses often show a mylonitic fabric, with clasts of Kfs stretched  
464 and rotated. In these rocks, S-C structures suggest top-the S/SW sense of shear. A

465 mineral lineation  $L_{m(U-GHS)}$  is locally defined by Bt, Sil, Sil-rich nodules (Fig. 6d) and/or  
466 Fsp, plunging parallel to the  $S_{m(U-GHS)}$  dip. The dominant  $S_{m(U-GHS)}$  is deformed by  
467 open to tight folds, with fold axes often striking NE-SW and axial planes plunging  
468 moderately to the north. In several outcrops, the  $S_{m(U-GHS)}$  is cross-cut by discrete top-  
469 to-the-south shear band cleavages, with white mica growing along the C-planes (Fig.  
470 7f).

471

## 472 **4.2 Petrography and mineral chemistry**

473 Microstructural features of samples 15-19, 15-28b, 15-26b, 15-38 and 14-12 are  
474 briefly discussed in this section, whereas those of the other samples (14-27a, 14-03,  
475 14-25b, 14-24, 14-44a, 14-61b, 14-71, 14-52, 14-08a) are presented by Rapa et al.  
476 (2016) and are summarized in Table 1. Mineral chemistry for all the samples is  
477 summarized in Table 2. Garnet chemical profiles of all the samples are given in Fig.  
478 S2a-d.

479

### 480 **4.2.1 Sample 15-19: Bt + Wm + Grt micaschist (LHS)**

481 Sample 15-19 is a fine-grained micaschist, consisting of Bt, Wm, Grt, Qz, Pl, Chl and  
482 accessory Ilm and Tur. The well-developed foliation ( $S_{2(LHS)}$ ) is defined by the  
483 preferred orientation of Bt and Wm, concentrated in continuous sub-mm-thick layers,  
484 alternating with discontinuous mm-thick layers rich in Qz and Pl (Fig. 8a). Locally, Qz  
485 aggregates, few-mm in thickness and with a granoblastic structure, could represent  
486 boudinated and transposed, pre- $S_{2(LHS)}$  Qz veins. Grt porphyroblasts (up to 2 mm in  
487 diameter) are dispersed in the matrix; they have a skeletal habit and are partly  
488 wrapped by the main foliation. Grt includes an internal rotated foliation ( $S_{1(LHS)}$ : snow-  
489 ball microstructure) defined by the alignment of Qz, Pl and Ilm. Pl is abundant and

490 often shows a granoblastic habit (Fig. S1c); larger porphyroblasts locally overgrow  
491 the main foliation. Large Chl and Wm flakes statically overgrow  $S_{2(LHS)}$  (Fig. S1d); Chl  
492 also replaces Bt and Grt rims (Fig. 8a).

493

#### 494 **4.2.2 Sample 15-28b: Bt + Wm + Grt + Ky + St micaschist (LHS)**

495 Sample 15-28b is a fine-grained two-mica phyllitic micaschist, consisting of Qz, Grt,  
496 Wm, Bt, Ky, St and accessory Gr, Tur and Ilm. The main schistosity ( $S_{2(LHS)}$ ) is  
497 defined by the preferred orientation of Wm and Bt in continuous sub-mm-thick layers  
498 alternating with discontinuous mm-thick Qz domains (Fig. 8b).  $S_{2(LHS)}$  transposes an  
499 older foliation ( $S_{1(LHS)}$ ) preserved in few microlithons and defined by both Wm and Bt  
500 (Fig. 8c). The main foliation is further crenulated and overprinted by a later, pluri-mm  
501 spaced planar foliation ( $S_{3(LHS)}$ ).  $S_{3(LHS)}$  is defined by Wm and Bt (Fig. S1e) and  
502 developed at high angle with respect to  $S_{2(LHS)}$ . Grt porphyroblasts are centimetric in  
503 size (up to 1 cm in diameter, Fig. 8b); they are idioblastic in the micaceous layers,  
504 while they have a skeletal habit in the Al-poor, quartzitic domains. Grt includes an  
505 internal foliation defined by Qz, Ilm, Gr and Wm, which is continuous with the external  
506  $S_{2(LHS)}$ ; it also includes St and minor Ky at its rims (Fig. 8c). St and Ky occur both as  
507 inclusions in the Grt rims and in the matrix; St includes Qz, Wm, Ilm and Gr. Ky in the  
508 matrix may include Qz and Ilm.

509

#### 510 **4.2.3 Sample 15-26b: Bt + Wm + Grt gneissic micaschist (LHS-Ramgarh Thrust** 511 **Sheet)**

512 Sample 15-26b is a medium-grained micaschist, consisting of Qz, Pl, Bt, Grt, minor  
513 Wm, accessory Rt and Ilm and minor late Chl and Sil. The main foliation ( $S_{2(LHS)}$ ) is  
514 defined by the preferred orientation of Bt and Wm concentrated in continuous, mm-

515 thick layers, alternating with few-mm-thick discontinuous Qz + Pl domains (Fig. 8d).  
516 Grt porphyroblasts (up to 2 mm in diameter) are abundant and dispersed in the  
517 matrix. They are partially wrapped by the main foliation and include Qz, Rt, Ilm and  
518 minor Bt, Wm and Pl (Fig. 8e). Grt rims are typically in equilibrium contacts with the  
519 matrix. Pl is in equilibrium with the  $S_{2(LHS)}$ ; it rarely includes Qz, Bt, Wm and Rt. An  
520 acicular aluminosilicate, possibly Sil, locally grows at the Pl–Wm interfaces; in the  
521 same microstructural position, symplectites consisting of Qz + Kfs rarely occur. Rt  
522 and Ilm are present both as inclusions in Grt and in the matrix and Ilm often replaces  
523 Rt in the matrix; rare Chl replaces Bt and Grt rims.

524

525 **4.2.4 Sample 15-38: Wm + Bt + Ky + St micaschist, with porphyroblastic Grt**  
526 **(Lower-GHS)**

527 Sample 15-38 is a coarse-grained micaschist consisting of Wm, Qz, Grt, Bt, Pl and  
528 minor Ky and St, with accessory Rt, Ilm and Turm. The main foliation ( $S_{2(L-GHS)}$ ) is  
529 defined by the preferred orientation of Wm and Bt flakes concentrated in pluri-mm  
530 continuous layers, alternating with mm-thick Qz and Pl domains.

531 Grt occurs both as large porphyroblasts (up to 4 mm in diameter) partially wrapped  
532 by the main foliation (Fig. 8f), and as small idioblasts (up to 1 mm in diameter) that  
533 show equilibrium relationships with Wm and Bt (Fig. S1f). Grt porphyroblasts are  
534 crowded with inclusions (Grt cores: Qz, Pl, Wm and minor Bt, Rt and Ilm; Grt rims:  
535 Qz, Wm, Pl, minor Bt and St, Rt and Ilm; Fig. S1h).

536 Locally, a later generation of Wm occurs as large flakes (up to 2 mm) overgrowing  
537  $S_{2(L-GHS)}$ . Ky is scarce, but where present it occurs as large bladed flakes (up to 3 mm  
538 in length) oriented generally parallel to the main foliation. Ky is always replaced by  
539 Wm (Fig. 8g) and/or Pl at its rims and it locally includes Bt. St is also scarce; it occurs

540 both as inclusions in Grt rims (Fig. S1h) and in the matrix as crystals up to 2 mm in  
541 length and including Pl, Qz and Rt (Fig. 8g). Pl is abundant, occurs as subhedral  
542 crystals and it locally includes Qz (Fig. S1g). Rare Sil replaces Grt rims (Fig. S1h).  
543 Accessory Rt and minor Ilm occur both as inclusions in Grt and in the matrix. Rt is  
544 often replaced by Ilm (Fig. S1h).

545

#### 546 **4.2.5 Sample 14-12: Bt + Grt + Sil migmatite (Upper-GHS)**

547 Sample 14-12 is a medium-grained Bt + Sil + Grt + Pl + Kfs + Qz migmatitic gneiss,  
548 with late Wm and accessory Ilm. It is characterized by a banded structure (Fig. 8h)  
549 defined by Bt + Sil + Qz ± Grt mm-thick mesocratic domains, alternating with Qz +  
550 Pl + Kfs ± Sil ± Bt pluri-mm leucocratic domains. The main foliation ( $S_{m(U-GHS)}$ ) is  
551 parallel to the compositional layering and is defined by the preferred orientation of Bt  
552 lepidoblasts and fibrolitic Sil. Grt porphyroblasts (up to 2 mm in diameter) are skeletal  
553 and contain large polymineralic inclusions of Qz + Bt + Pl (Fig. 8i). Bt in the matrix is  
554 locally overgrown by large flakes of Wm. Pl and Kfs are mainly concentrated in the  
555 leucocratic domains though Pl is also observed replacing Grt rims (Fig. 8i).  
556 Myrmekitic structures occur at the interface between Kfs and Pl (Fig. S1i).

557 The mesocratic domains are characterized by the occurrence of Bt + Qz + Sil + Pl  
558 symplectites developed at the expenses of Kfs and of Wm + Qz + Pl symplectites  
559 developed at the expenses of Kfs and Grt (Fig. S1l).

560

#### 561 **4.3. P-T evolution of LHS, LHS-Ramgarh Thrust Sheet, Lower-GHS and Upper-** 562 **GHS units**

563 The P-T evolution of the studied samples was constrained using two independent  
564 methods: optimal thermobarometry (i.e. AvPT) and the pseudosection approach. Our



565 aim was to test if tectonometamorphic discontinuities might be detected using the  
566 relatively fast AvPT approach, which allows application of relative thermobarometry  
567 on a large number of samples, as an alternative to the more laborious and time  
568 consuming pseudosection approach.

569

#### 570 **4.3.1 Optimal thermobarometry**

571 **LHS** - In the LHS phyllitic micaschists (samples 15-19, 14-27a and 15-28b), both the  
572 prograde and the peak equilibrium assemblages (defining the  $S_{1(LHS)}$  and the  $S_{2(LHS)}$   
573 foliations, respectively) define enough equilibria to converge to an AvPT result (§3.3).  
574 The obtained *P-T* results are similar for all the samples: the prograde  $S_{1(LHS)}$   
575 development is estimated at about 540°C and 6.6-7.0 kbar, while peak *P-T*  
576 conditions occurred at about 590-600°C and 7.1-8.2 kbar (Fig. 9a,b, Fig. 10a,b and  
577 Table 3). Overall, the LHS samples recorded a prograde *P-T* evolution characterized  
578 by an increase in both *P* and *T* up to the peak of metamorphism, corresponding to a  
579 *T/P* ratio of 80 °C/kbar (Table 4b).

580 **LHS-Ramgarh Thrust Sheet** - Sample 15-26b, exposed within the Ramgarh Thrust  
581 Sheet just below the MCT, gives higher *P-T* conditions for both the prograde and  
582 peak assemblages, with respect to the other LHS samples. Specifically, prograde *P-*  
583 *T* conditions are estimated at about 585°C, 7.8 kbar, while peak *P-T* conditions  
584 occurred at 600°C, 8.8 kbar (Fig. 9a,b, Fig. 10a,b and Table 3). The geometry of the  
585 prograde *P-T* path is nevertheless similar to that of the other LHS samples, but the  
586 *T/P* ratio is lower (69 °C/kbar, Table 4b).

587 **Lower-GHS** - The Lower-GHS metapelitic samples (14-03, 14-25b, 14-24, 15-38, 14-  
588 44a, 14-61b, 14-71) recorded peak *P-T* conditions in the range 660-710°C, 8.3-9.8  
589 kbar, with a slight increase in both *P* and *T* proceeding structurally upward in the

590 transect (Fig. 9c-f, Fig. 10a,b and Table 3). The structurally lowermost samples (14-  
591 03, 14-25b and 15-38) preserve evidence of their prograde history at 585-640°C, 6.4-  
592 7.8 kbar (Fig. 9c-d, Table 3). The structurally higher samples do not preserve  
593 evidence of their prograde evolution. Lowering the  $a_{\text{H}_2\text{O}}$  to 0.9 to simulate the  
594 occurrence of incipient partial melting at peak conditions, would result in a decrease  
595 of both T and P of about 10-15°C, 0.1-0.5 kbar (Table 3). The estimated peak  
596 metamorphic conditions correspond to a T/P ratio of about 76 °C/kbar (Table 4b).  
597 The structurally uppermost sample 14-52 records unusually high peak P-T conditions  
598 ( $850 \pm 68^\circ\text{C}$ ,  $11.3 \pm 2.7$  kbar), but also shows the highest uncertainties. These P-T  
599 conditions are unrealistic because this sample does not show evidence of partial  
600 melting (Rapa et al., 2016). It is likely that AvPT failed in calculating peak P-T  
601 conditions for this sample because it does not contain Wm, probably deriving from a  
602 Bt-rich protolith.

603 **Upper-GHS** - The Upper-GHS samples (14-08a and 14-12) do not preserve relics of  
604 their prograde history, and experienced various degrees of partial melting. These  
605 samples recorded peak P-T conditions of 800-815°C, ~6 kbar (Fig. 9c,d, Fig. 10a,b  
606 and Table 3), well within the Sil-stability field, defining a T/P ratio of 134 °C/kbar (Fig.  
607 9c,d, Table 3 and Table 4b).

608 The uncertainties ( $2\sigma$  values) associated to the AvPT results are generally greater  
609 than  $\pm 20^\circ\text{C}$  and  $\pm 1$  kbar; these relatively large uncertainties might be due to several  
610 factors, including analytical uncertainties or uncertainties in the thermodynamic data  
611 and in the activity-composition relationships (e.g. Fraser et al., 2000). However, it is  
612 worth noting that *P-T* conditions independently constrained using the pseudosection  
613 approach (see Rapa et al., 2016 and the following Section 4.3.2) plot very close to, or  
614 totally within the uncertainties of, the AvPT results (Fig. 10a,b).

615

### 616 **4.3.2 P-T pseudosections**

617 P-T pseudosections have been modeled by Rapa et al. (2016) for nine of the 14  
618 samples investigated in this study. Additional P-T pseudosections have been  
619 calculated in this study for sample 15-26b, because Rapa et al. (2016) didn't  
620 investigate the P-T evolution of the LHS-Ramgarh Thrust Sheet. The bulk-rock  
621 composition of sample 15-26b was calculated by combining mineral modes and  
622 compositions (see Rapa et al., 2016 for methodology). Two pseudosections have  
623 been calculated for this sample to account for the fractionation effects on the bulk  
624 composition due to the growth of zoned garnet porphyroblasts. The pseudosection  
625 calculated for the unfractionated bulk composition (Fig. 11a,b) gives information  
626 about the mineral assemblage stable during the prograde growth of Grt core, which  
627 includes Bt, Wm, Pl, Rt  $\pm$  Ilm. This assemblage is stable in the Bt  $\pm$  Chl + Pl + Ms  $\pm$   
628 Pg + Grt + Qz + Rt + H<sub>2</sub>O fields, at T>450°C. Grt core compositional isopleths  
629 (XMg=0.09-0.11, XCa=0.17-0.20, XMn=0.09-0.07; Fig. S2a) further constrain the P-T  
630 conditions of the prograde Grt growth at T=550-575°C and P=7.5-8.5 kbar, in the Bt +  
631 Chl + Pl + Ms + Grt + Qz + Rt field. Chl has not been observed included in Grt in this  
632 sample because it was completely consumed during prograde metamorphism.  
633 Growth of Grt rim in the quini-variant Bt + Pl + Ms + Grt + Qtz + Rt field (Fig. 11c) is  
634 consistent with the interpreted equilibrium between Grt rim and Bt, Ms, Pl and Rt ( $\pm$   
635 Ilm). Compositional isopleths (XMg=0.13-0.14; XCa=0.16-0.14; XMn=0.03-0.04;  
636 Fig. S2b) constrain the growth of Grt rim at peak P-T conditions of 620-650°C, 8.7-  
637 10.4 kbar (Fig. 11c, Table 4a). Both Grt core and Grt rim are predicted to grow at  
638 sub-solidus conditions (Fig. 11d), in agreement with microstructural observations.

639

## 640 5. DISCUSSION

### 641 5.1 Comparison between AvPT and pseudosection results

642 The comparison between peak P-T conditions constrained using the AvPT method  
643 and those constrained using the pseudosection approach is reported in Table 4 and  
644 Fig. 10a,b. The two methods give consistent results relative to one another, although  
645 the absolute P-T values are slightly different; peak P-T conditions estimated with the  
646 AvPT method are generally lower than those estimated using the pseudosection  
647 approach (Fig. 10a,b). Peak temperatures constrained with both methods gradually  
648 increase structurally upward, passing from 590-600°C in the LHS to 610-640°C in the  
649 LHS-Ramgarh Thrust Sheet, 700-740°C in the Lower-GHS and 780-810°C in the  
650 Upper-GHS. In addition, both methods highlight pressure breaks in both the LHS and  
651 GHS sequences. Specifically, peak pressures in the LHS-Ramgarh Thrust Sheet  
652 (8.8-9.6 kbar) are higher than those registered in the lowermost LHS (7.4-7.5 kbar),  
653 whereas peak pressures in the Upper-GHS (6.1-7.8 kbar) are lower than those  
654 registered in the lowermost Lower-GHS (9.3-10 kbar). This implies significantly  
655 different T/P ratios for the four units (see the following section 5.2). The T/P ratios  
656 obtained with the AvPT method are remarkably similar to those obtained using the  
657 pseudosection approach as concerning the LHS, LHS-Ramgarh Thrust Sheet and  
658 Lower-GHS samples (Table 4); the AvPT results for Upper-GHS samples define a  
659 higher T/P ratio with respect to that constrained using pseudosections ( $134 \pm 41$   
660 °C/kbar vs.  $101 \pm 12$  °C/kbar), due to the large uncertainties in the AvPT estimates.  
661 Both methods are therefore useful to recognise rock packages characterized by  
662 different peak P-T conditions, although uncertainties related to the AvPT results are  
663 larger than those related to the pseudosection results (i.e. absolute P-T values  
664 obtained using pseudosections are more reliable than those obtained using AvPT).

665 The AvPT method is faster to apply than the pseudosection approach, thus allowing  
666 to focalize the following more precise – but also more time consuming, more  
667 expensive and more complex – studies (e.g. pseudosections, geochronology, etc.)  
668 on specific and selected areas only. Conversely, the main advantage of the  
669 pseudosection approach over the AvPT method is the possibility of reconstructing the  
670 whole P-T evolution of the studied samples (i.e. prograde and/or retrograde *P-T*  
671 evolution), which can outline the differences and similarities of *P-T* paths in a set of  
672 samples otherwise only grouped by coherent peak *P-T* conditions.

673

## 674 **5.2 Petrological and structural criteria for identifying tectonometamorphic** 675 **discontinuities within the LHS and the GHS**

676 Peak *P-T* conditions obtained for the studied samples using the pseudosection  
677 approach and the AvPT method highlight the existence of four different T/P ratio  
678 populations of  $80 \pm 11$  °C/kbar (LHS),  $66 \pm 7$  °C/kbar (LHS-Ramgarh Thrust Sheet),  
679  $73 \pm 1$  °C/kbar (Lower-GHS) and  $101 \pm 12$  °C/kbar (Upper-GHS), respectively (Fig.  
680 10c and Table 4). These values are partially overlapped within errors (Fig. 10c),  
681 because of the relatively large errors associated to the weighted average values  
682 estimated for each population. However, these errors would be reduced, and the  
683 difference between populations would be consequently enhanced, if more samples  
684 are considered for each unit (e.g. compare the small error associated to the Lower-  
685 GHS, for which eight samples have been considered, with the relatively large error  
686 associated to the LHS-Ramgarh Thrust Sheet, for which only one sample was  
687 considered). Furthermore, even considering the partially overlapped T/P ratio values,  
688 the different populations can be easily recognized by combining the T/P ratios with  
689 the absolute T estimates (i.e.  $T < 650$ °C for the LHS and LHS-Ramgarh Thrust

690 Sheet;  $T > 650^{\circ}\text{C}$  for the Lower-GHS). Finally, it is worth noting that our results are in  
691 good agreement with those calculated using the P-T results of Kohn (2008) for  
692 samples collected from the same structural levels in the Langtang region (ZL1-3:  $71 \pm$   
693  $6^{\circ}\text{C/kbar}$ ; ZL4:  $55 \pm 3^{\circ}\text{C/kbar}$ ; ZG1 and ZG2:  $63 \pm 3^{\circ}\text{C/kbar}$ ; ZG3 and ZG4:  $92 \pm 8$   
694  $^{\circ}\text{C/kbar}$ ; P-T data obtained using the conventional thermobarometry approach; see  
695 also Fig. 10), thus confirming the statistical difference between T, P and T/P ratios  
696 estimated for each unit. Rock packages recording different T/P ratios are also  
697 characterized by different P-T evolutions (see also Rapa et al., 2016) (Fig. 12). The  
698 P-T paths recorded by LHS and LHS-Ramgarh Thrust Sheet samples have a similar  
699 hairpin shape, although that of the LHS-Ramgarh Thrust Sheet unit is shifted towards  
700 higher P-T conditions. The Lower-GHS samples describe a clockwise P-T trajectory  
701 mostly in the Ky stability field. Their prograde evolution, characterized by an increase  
702 in both T and P, is only recorded by the structurally lower samples, whereas the  
703 retrograde evolution is well preserved in all the samples. The Upper-GHS samples  
704 recorded a clockwise P-T path, but in the Sil stability field, characterized by nearly  
705 isobaric heating associated with partial melting processes (Rapa et al., 2016).  
706 Overall, petrological data are consistent with the existence of three metamorphic  
707 discontinuities which separate the LHS from the LHS-Ramgarh Thrust Sheet (lower  
708 discontinuity), the LHS-Ramgarh Thrust Sheet from the Lower-GHS (intermediate  
709 discontinuity) and the Lower-GHS from the Upper-GHS (upper discontinuity).  
710 Mesostructural data show that the lower and intermediate metamorphic  
711 discontinuities also coincide with pervasive syn-metamorphic deformation (e.g.  
712 mylonitic foliation, mesoscopic shear zones, occurrence of different stretched  
713 lithological bodies) with a consistent top-to-the-south sense of shear, thus indicating  
714 that these metamorphic discontinuities also coincide with structural discontinuities.

715 Mesostructural data for the upper discontinuity are more ambiguous, because of the  
716 interplay between tectonic, melt-producing and melt-crystallizing processes which  
717 occurred in the high-grade, often migmatitic, Upper-GHS lithologies. However, a  
718 consistent top-to-the-south sense of shear is recorded by widespread asymmetric  
719 boudinage, asymmetry of folds and S-C structures.

720 The lower discontinuity outlined in the study area **can be identified with** the Ramgarh  
721 Thrust (Munsiari Thrust in Kohn, 2008), which separates a package of LHS rocks in  
722 its hanging wall (LHS-Ramgarh Thrust Sheet) that experienced peak metamorphism  
723 at higher P-T conditions (~635°C, 10 kbar) than the other LHS rocks in its foot wall  
724 that experienced peak metamorphism at lower P-T conditions (~600°C, 7.5 kbar).  
725 The intermediate discontinuity coincides with the MCT, which separates the LHS  
726 from the GHS. The MCT is marked by an abrupt increase in both peak P and T, up to  
727 740°C, 9.5-10.5 kbar over a structural distance of less than 2 km. The upper  
728 discontinuity is defined as Langtang Thrust (Kohn et al., 2005) and separates the  
729 Lower-GHS from the Upper-GHS, which experienced significantly different peak  
730 metamorphic conditions and P-T evolutions (Lower-GHS: 700-740°C, 9.5-10.5 kbar,  
731 prograde increase in both P and T in the kyanite stability field; Upper-GHS: 780-  
732 800°C, 7.5-8.0 kbar; nearly isobaric heating in the sillimanite stability field).

733

### 734 **5.3 Thrusting kinematics of the study area**

735 In the study area, the Ramgarh Thrust and MCT are sub-parallel, with a NW-SE trend  
736 north of Syabrubensi, becoming roughly N-S towards the south. Conversely, the  
737 strike of the Langtang Thrust changes from NW-SE to roughly E-W (Fig. 2). The  
738 spatial disposition of these three main structural and metamorphic discontinuities  
739 characterizes the tectonic architecture of the area. The north-dipping Lower-GHS is

740 few km thick in the Gatlang-Langtang region. It dips flattens progressively towards  
741 the Gosainkund-Helambu region where it is more broadly exposed (see also Rapa et  
742 al., 2016) and then it becomes south-dipping on the northern side of the synformal  
743 Kathmandu Nappe, in the Kathmandu area (Fig. 1 and Fig. 2). Geological and  
744 petrological constraints (Rapa et al., 2016 and references therein) support a  
745 Kathmandu Nappe configuration in which the Lower-GHS rocks are directly overlaid  
746 by a succession (Bhimpedi-Phulchauki group) interpreted as correlative to the TSS.  
747 The juxtaposition of this portion of TSS on the Lower-GHS occurs across a shear  
748 zone (Galchi shear zone of Webb et al., 2011), which corresponds to the southern  
749 prolongation of the STDS. It merges with the MCT along the northern margin of the  
750 Kathmandu Nappe (e.g. Johnson et al., 2001; Webb et al., 2011; He et al., 2015). As  
751 for other sectors of the Himalaya , this tectonometamorphic architecture is result from  
752 the development of multiple south-verging thrusts, including intra-GHS thrusting,  
753 juxtaposition of the GHS onto the LHS and the formation of foreland-directed LHS  
754 duplex structures at the regional scale (e.g. Schelling and Arita, 1991; Pearson and  
755 DeCelles, 2005; Khanal et al., 2015).

756 Detailed geochronological data (monazite U-Pb ages) presented by Kohn et al.  
757 (2004, 2005) and Kohn (2004, 2008) for the Gatlang-Langtang transect show that the  
758 age of peak metamorphism is progressively younger towards lower structural levels  
759 (Upper-GHS: 25-21 Ma; Lower-GHS: 24-17 Ma; LHS-Ramgarh Thrust Sheet: 13-10  
760 Ma; LHS: 4-3 Ma). Moreover, titanite U-Pb ages obtained from a Lower-GHS calc-  
761 silicate rock exposed in the adjacent Gosainkund-Helambu region consistently point  
762 to peak metamorphic ages of 19-20 Ma (Rapa et al., 2017). These ages support an  
763 in-sequence thrusting interpretation for all the tectonometamorphic discontinuities  
764 recognized in the area. The movement along the Ramgarh Thrust is constrained to



765 have occurred after the intra-GHS thrusting and the MCT activation (Kohn et al.,  
766 2004). The formation of the LHS duplexing can be constrained between 10-3 Ma and  
767 ended with the activation of the MBT to the south (<3 Ma). The  $D_{3(LHS)}$  folding event  
768 (roughly characterized by NE-SW striking axis) interpreted in this study, can be  
769 tentatively correlated with duplex formation. The present steep dips of the Ramgarh  
770 Thrust and MCT in the Langtang region may reflect a late tilting on the northern  
771 ramps during the in-depth emplacement of LHS thrust sheets and the growing of a  
772 large-scale antiform because of  $D_{3(LHS)}$  and  $D_{4(LHS)}$  interferences (Fig. 1).  
773 In this setting, the extensional features identified in the upper LHS and in the LHT-  
774 Ramgarh Thrust Sheet, developed mainly in a brittle-ductile regime, define an  
775 extensional regime parallel to the orogen during an overall shortening.

776

## 777 **6. Conclusions**

778 Overall, data and results presented in this paper demonstrate that petrological and  
779 structural analysis are capable of identifying tectonometamorphic discontinuities in  
780 the LHS and GHS, thus allowing their fast detection. Such discontinuities are marked  
781 by: (i) contrasting  $T/P$  ratios, peak P-T conditions and P-T paths in the footwall and  
782 hanging-wall; (ii) an increase in the intensity of deformation, with development of  
783 pervasive mylonitic fabrics and/or shear zones, in proximity to the discontinuity.  
784 Geochronological data are not necessarily required to identify such discontinuities,  
785 but become indispensable for the interpretation of their nature (e.g. in-sequence vs.  
786 out-of-sequence thrust) and for the reconstruction of kinematic models.

787

## 788 **ACKNOWLEDGEMENTS**

789 Fieldwork and laboratory work was supported by the University of Torino (Ricerca  
790 Locale, ex-60% -2014, 2015 funds: ROLF\_RILO\_15\_01, GROC\_RILO\_16\_01) and

791 Compagnia di San Paolo (University of Torino, Call 1, Junior PI Grant:  
792 TO\_Call1\_2012\_0068), by the Italian Ministry of University and Research (PRIN  
793 2011: 2010PMKZX7) and by Ev-K2-CNR (SHARE Project) in collaboration with the  
794 Nepal Academy of Science and Technology. K. Larson and an anonymous reviewer  
795 are kindly acknowledged for their constructive comments which improved the  
796 manuscript.

797

799 **REFERENCES**

- 800 Ambrose, T.K., Larson, K.P., Guilmette, C., Cottle, J.M., Buckingham, H., Rai, S.,  
801 2015. Lateral extrusion, underplating, and out-of-sequence thrusting within the  
802 Himalayan metamorphic core, Kanchenjunga, Nepal. *Lithosphere* 7, 441-464.
- 803 Auzanneau, E., Schmidt, M.W., Vielzeuf, D., Connolly, J.A.D., 2010. Titanium in  
804 phengite: a geobarometer for high temperature eclogites. *Contributions to*  
805 *Mineralogy and Petrology* 159, 1–24.
- 806 Carosi, R., Montomoli, C., Visonà, D., 2007. A structural transect in the Lower Dolpo:  
807 insights on the tectonic evolution of Western Nepal. *Journal of Asian Earth*  
808 *Science* 29, 407–423.
- 809 Carosi, R., Montomoli, C., Rubatto, D., Visonà, D., 2010. Late oligocene high-  
810 temperature shear zones in the core of the Higher Himalayan Crystallines (Lower  
811 Dolpo, western Nepal). *Tectonics* 29, TC4029.
- 812 Catlos, E.J., Harrison, T. M., Kohn, M.J., Grove, M., Ryerson, F.J., Manning, C.E.,  
813 Upreti, B. N., 2001. Geochronologic and thermobarometric constraints on the  
814 evolution of the Main Central Thrust, central Nepal Himalaya. *Journal of*  
815 *Geophysical Research: Solid Earth* 106, 16177– 16204.
- 816 Catlos, E.J., Harrison, T. M., Manning, C.E., Grove, M., Rai, S.M., Hubbard, S.M.,  
817 Upreti, B.N., 2002. Records of the evolution of the Himalayan orogen from in situ  
818 Th–Pb ion microprobe dating of monazite: Eastern Nepal and western Garhwal.  
819 *Journal of Asian Earth Science* 20, 459-479.
- 820 Cenki, B., Kriegsman, L.M., Braun, I., 2002. Melt-producing and melt-consuming  
821 reactions in the Achankovil cordierite gneisses, South India. *Journal of*  
822 *Metamorphic Geology* 20, 543–561.

823 Coggon, R., Holland, T.J.B., 2002. Mixing properties of phengitic micas and revised  
824 garnet–phengite thermobarometers. *Journal of Metamorphic Geology* 20, 683–  
825 696.

826 Connolly, J.A.D., 1990. Multivariable phase diagrams: an algorithm based on  
827 generalized thermodynamics. *American Journal of Science* 290, 666–718.

828 Connolly, J.A.D., 2009. The geodynamic equation of state: what and how.  
829 *Geochemistry Geophysics Geosystems* 10, Q10014.

830 Daniel, C.G., Hollister, L., Parrish, R.R., Grujic, D., 2003. Exhumation of the Main  
831 Central thrust from lower crustal depths, Eastern Bhutan Himalaya. *Journal of*  
832 *Metamorphic Geology* 21, 317–334.

833 Davidson, C., Grujic, D., Hollister, L., Schmid, S.M., 1997. Metamorphic reaction  
834 related to decompression and synkinematic intrusion of leucogranite, high  
835 Himalayan Crystallines, Bhutan. *Journal of Metamorphic Geology* 15, 593–612.

836 DeCelles, P.G., Robinson, D.M., Quade, J., Ojha, T.P., Garzzone, C.N., Copeland, P.,  
837 Upreti, B.N., 2001. Stratigraphy, structure and tectonic evolution of the Himalayan  
838 fold–thrust belt in western Nepal. *Tectonics* 20, 487–509.

839 Fraser, G., Worley, B., Sandiford, M., 2000. High-precision geothermobarometry  
840 across the High Himalayan metamorphic sequence, Langtang Valley, Nepal.  
841 *Journal of Metamorphic Geology* 18, 665–681.

842 Gaetani, M., Garzanti, E., 1991. Multicyclic history of the northern India continental  
843 margin (north- western Himalaya). *AAPG Bulletin* 75, 1427–1446.

844 Gansser, A., 1983, *Geology of the Bhutan Himalaya*: Birkhäuser Verlag, Basel, 181  
845 pp.

846 Godin, L., Grujic, D., Law, R.D., Searle, M. P., 2006. Channel flow, ductile extrusion  
847 and exhumation in continental collision zones: an introduction. In: Law, R.D.,

848 Searle, M.P., Godin, L. (Eds.) Channel flow, ductile extrusion and exhumation in  
849 continental collision zones. Geological Society of London Special Publications  
850 268, pp. 1–23.

851 Goscombe, B., Hand, M., 2000. Contrasting P-T paths in the Eastern Himalaya,  
852 Nepal: inverted isograds in a paired metamorphic mountain belt. *Journal of*  
853 *Petrology* 41, 1673–1719.

854 Goscombe, B., Gray, D., Hand, M., 2006. Crustal architecture of the Himalayan  
855 metamorphic front in eastern Nepal. *Gondwana Research* 10, 232–255.

856 Groppo, C., Rolfo, F., Lombardo, B., 2009. P-T evolution across the Main Central  
857 Thrust Zone (Eastern Nepal): hidden discontinuities revealed by petrology. *Journal*  
858 *of Petrology* 50, 1149–1180.

859 Groppo, C., Rubatto, D., Rolfo, F., Lombardo, B. , 2010. Early Oligocene partial  
860 melting in the Main Central Thrust Zone (Arun Valley, eastern Nepal Himalaya).  
861 *Lithos* 118, 287-301.

862 Groppo, C., Rolfo, F., Indares, A., 2012. Partial melting in the Higher Himalayan  
863 Crystallines of Eastern Nepal: the effect of decompression and implications for the  
864 “channel flow” model. *Journal of Petrology* 53, 1057–1088.

865 Groppo, C., Rolfo, F., Mosca, P., 2013. The cordierite-bearing anatectic rocks of the  
866 Higher Himalayan Crystallines (eastern Nepal): low-pressure anatexis, melt-  
867 productivity, melt loss and the preservation of cordierite. *Journal of metamorphic*  
868 *Geology* 31, 187–204.

869 Guillot, S., 1999. An overview of the metamorphic evolution of Central Nepal. *Journal*  
870 *of Asian Earth Sciences* 17, 713-725.

871 Harrison, T.M., Ryerson, F.J., Le Fort, P., Yin, A., Lovera, O.M., Catlos, E.J., 1997. A  
872 late Miocene–Pliocene origin for the Central Himalayan inverted metamorphism.  
873 Earth and Planetary Science Letters 146, E1–E7.

874 He, D., Webb, A.A.G., Larson, K.P., Martin, A.J., Schmitt, A.K., 2015. Extrusion vs.  
875 duplexing models of Himalayan mountain building. 3: Duplexing dominates from  
876 the Oligocene to Present. International Geology Review 57, 1–27.

877 Hodges, K., 2000. Tectonics of Himalaya and southern Tibet from two perspectives.  
878 Geological Society of American Bulletin 112, 324–350.

879 Holland, T.J.B., Powell, R., 1998. An internally consistent thermodynamic data set for  
880 phases of petrologic interest. Journal of Metamorphic Geology 16, 309–343.

881 Holland, T.J.B., Powell, R., 2001. Calculation of phase relations involving  
882 haplogranitic melts using an internally consistent thermodynamic dataset. Journal  
883 of Petrology 42, 673–683.

884 Holland, T.J.B., Powell, R., 2011. An improved and extended internally consistent  
885 thermodynamic dataset for phases of petrological interest, involving a new equation  
886 of state for solids. Journal of Metamorphic Geology 29, 333–383.

887 Holland, T., Baker, J., Powell, R., 1998. Mixing properties and activity-composition  
888 relationships of chlorites in the system MgO-FeO-Al<sub>2</sub>O<sub>3</sub>-SiO<sub>2</sub>-H<sub>2</sub>O. European  
889 Journal of Mineralogy 10, 395–406.

890 Holness, M.B., Clemens, J.D., 1999. Partial melting of the Appin Quartzite driven by  
891 fracture controlled H<sub>2</sub>O infiltration in the aureole of the Ballachulish Igneous  
892 Complex, Scottish Highlands. Contributions to Mineralogy and Petrology 136,  
893 154–168.

894 Holness, M.B., Sawyer, E.W., 2008. On the pseudomorphing of melt-filled pores  
895 during the crystallization of migmatites. Journal of Petrology 49, 1343–1363.

896 Iaccarino, S., Montomoli, C., Carosi, R., Massonne, H-J., Visonà, D., 2017. Geology  
897 and tectonometamorphic evolution of the Himalayan metamorphic core: insights  
898 from the Mugu Karnali transect, Western Nepal (Central Himalaya). *Journal of*  
899 *Metamorphic Geology* 35, 301-325.

900 Imayama, T., Takeshita, T., Arita, K., 2010. Metamorphic P–T profile and P–T path  
901 discontinuity across the far-eastern Nepal Himalaya: investigation of channel flow  
902 models. *Journal of Metamorphic Geology* 28, 527–549.

903 Imayama, T., Takeshita, T., Yi, K., Cho, D.-L., Kitajima, K., Tsutsumi, Y., Kayama,  
904 M., Nishido, H., Okumura, T., Yagi, K., Itaya, T., Sano, Y., 2012. Two-stage partial  
905 melting and contrasting cooling history within the Higher Himalayan Crystalline  
906 Sequence in the far-eastern Nepal Himalaya. *Lithos* 134-135, 1–22.

907 Inger, S., Harris, N.B.W., 1992. Tectonothermal evolution of the High Himalayan  
908 Crystalline Sequence, Langtang Valley, northern Nepal. *Journal of Metamorphic*  
909 *Geology* 10, 439–452.

910 Jessup, M.J., Law, R.D., Searle, M.P., Hubbard, M.S., 2006. Structural evolution and  
911 vorticity of flow during extrusion and exhumation of the Greater Himalayan Slab,  
912 Mount Everest Massif, Tibet/Nepal: implications for orogen-scale flow partitioning.  
913 In: Law, R.D., Searle, M.P., Godin, L. (Eds.), *Channel Flow, Extrusion, and*  
914 *Exhumation in Continental Collision Zones*. Geological Society of London Special  
915 Publications 268, pp. 379-414.

916 Johnson, M. R. W., Oliver, G. J. H., Parrish, R. R., Johnson, S. P., 2001.  
917 Synthrusting metamorphism, cooling, and erosion of the Himalayan Kathmandu  
918 Complex, Nepal. *Tectonics* 20, 394–415.

919 Khanal, S., Robinson, D.M., Kohn, M.J., Mandal, S., 2015. Evidence for a far-  
920 traveled thrust sheet in the Greater Himalayan thrust system, and an alternative  
921 model to building the Himalaya. *Tectonics* 34, 31–52.

922 Kohn M.J., 2004. Oscillatory- and sector-zoned garnets record cyclic (?) rapid  
923 thrusting in central Nepal. *Geochemistry Geophysics Geosystems* 5, Q12014.

924 Kohn, M.J., 2008. PTt data from central Nepal support critical taper and repudiate  
925 large-scale channel flow of the Greater Himalayan Sequence. *Geological Society*  
926 *of America Bulletin* 120, 259–273.

927 Kohn, M.J., Wieland, M.S., Parkinson, C.D. Upreti, B.N., 2004. Miocene faulting at  
928 plate tectonic velocity in the Himalaya of central Nepal. *Earth and Planetary*  
929 *Science Letters* 228, 299–310.

930 Kohn, M.J., Wieland, M., Parkinson, C.D., Upreti, B.N., 2005. Five generation of  
931 monazite in Langtang gneisses: implication for chronology of the Himalayan  
932 metamorphic core. *Journal of Metamorphic Geology* 23, 399–406.

933 Kohn, M.J., Paul, S.K., Corrie, S.L., 2010. The lower Lesser Himalayan Sequence: A  
934 Paleoproterozoic arc on the northern margin of the Indian plate. *Geological Society*  
935 *of America Bulletin* 122, 323-335.

936 Kriegsman, L.M., Ivarez-Valero, A.M., 2010. Melt-producing versus melt-consuming  
937 reactions in pelitic xenoliths and migmatites. *Lithos* 116, 310–320.

938 Larson, K.P., Cottle, J.M., 2014. Midcrustal discontinuities and the assembly of the  
939 Himalayan mid-crust. *Tectonics* 33, 718–740.

940 Larson, K.P., Godin, L., Price, R.A., 2010. Relationships between displacement and  
941 distortion in orogens: linking the Himalayan foreland and hinterland in central  
942 Nepal. *Geological Society of America Bulletin* 122, 1116–1134.



943 Larson, K.P., Gervais, F., Kellett, D.A., 2013. A P–T–t–D discontinuity in east-central  
944 Nepal: Implications for the evolution of the Himalayan mid-crust. *Lithos* 179, 275–  
945 292.

946 Larson, K.P., Ambrose, T.K., Webb, A.G., Cottle, J.M., Shrestha, S., 2015.  
947 Reconciling Himalayan midcrustal discontinuities: the Main Central thrust system.  
948 *Earth and Planetary Science Letters* 429, 139–146.

949 Law, R.D., Searle, M. P., Simpson, R.L., 2004. Strain, deformation temperatures and  
950 vorticity of flow at the top of the Greater Himalayan Slab, Everest Massif, Tibet.  
951 *Journal of the Geological Society, London* 161, 305–320.

952 Le Fort, P., Rai, S.M., 1999. Pre-Tertiary felsic magmatism of the Nepal Himalaya.  
953 Recycling of continental crust. *Journal of Asian Earth Sciences* 17, 607–628.

954 Lombardo, B., Pertusati, P., Borghi, A., 1993. Geology and tectono-magmatic  
955 evolution of the eastern Himalaya along the Chomolungma–Makalu transect. In:  
956 Treloar, P.J., Searle, M.P. (Eds.), *Himalayan Tectonics*. Geological Society of  
957 London Special Publication 74, 341–355.

958 Macfarlane, A.M., 1993. Chronology of tectonic events in the crystalline core of the  
959 Himalaya, Langtang National Park, central Nepal. *Tectonics* 12, 1004–1025.

960 Macfarlane, A.M., 1995. An evaluation of the inverted metamorphic gradient at  
961 Langtang National Park, Central Nepal, Himalaya. *Journal of Metamorphic  
962 Geology* 13, 595–612.

963 Macfarlane, A.M., Hodges, K.V., Lux, D., 1992. A structural analysis of the Main  
964 Central Thrust zone, Langtang National Park, central Nepal Himalaya. *Geological  
965 Society of America Bulletin* 104, 1389–1402.

966 Martin, A.J., 2017. A review of definitions of the Himalayan Main Central Thrust.  
967 *International Journal of Earth Sciences* 106, 2131–2145.

968 Martin, A.J., DeCelles, P.G., Gehrels, G.E., Patchett, P.J., Isachsen, C., 2005.  
969 Isotopic and structural constraints on the location of the Main Central thrust in the  
970 Annapurna Range, central Nepal Himalaya. *Geological Society of America Bulletin*  
971 117, 926–944.

972 McQuarrie, N., Robinson, D.M., Long, S.P., Tobgay, T., Grujic, D., Gehrels, G.E.,  
973 Ducea, M., 2008. Preliminary stratigraphic and structural architecture of Bhutan:  
974 implications for the along strike architecture of the Himalayan system. *Earth and*  
975 *Planetary Science Letters* 272, 105–117.

976 Montomoli, C., Iaccarino, S., Carosi, R., Langone, A., Visonà, D., 2013.  
977 Tectonometamorphic discontinuities within the Greater Himalayan Sequence in  
978 Western Nepal (Central Himalaya): Insights on the exhumation of crystalline rocks.  
979 *Tectonophysics* 608, 1349–1370.

980 Montomoli, C., Carosi, R., Iaccarino, S., 2015. Tectonometamorphic discontinuities in  
981 the Greater Himalayan Sequence: a local or a regional feature? *Geological*  
982 *Society London Special Publications* 412, 25–41.

983 Mosca, P., Groppo, C., Rolfo, F., 2012. Structural and metamorphic features of the  
984 Main Central Thrust Zone and its contiguous domains in the eastern Nepalese  
985 Himalaya. *Journal of Virtual Explorer, Electronic Edition* 41, paper 2.

986 Newton, R.C., Charlu, T.V., Kleppa, O.J., 1980. Thermochemistry of the high  
987 structural state Pls. *Geochimica et Cosmochimica Acta* 44, 933–941.

988 Pearson, O.N., 2002. Structural evolution of the central Nepal fold-thrust belt and  
989 regional tectonic and structural significance of the Ramgarh thrust. Ph.D.,  
990 University of Arizona.

991 Pearson, O.N., DeCelles, P.G., 2005. Structural geology and regional tectonic  
992 significance of the Ramgarh Thrust, Himalayan fold-thrust belt of Nepal. *Tectonics*  
993 24, TC4008.

994 Pognante, U., Benna, P., 1993. Metamorphic zonation, migmatization, and  
995 leucogranites along the Everest transect (eastern Nepal and Tibet): record of an  
996 exhumation history. In: Treloar, P.J., Searle, M.P. (Eds.), *Himalayan Tectonics*.  
997 Geological Society of London Special Publications 74, 323-340.

998 Pouchou, J.L., Pichoir, F., 1988. Determination of mass absorption coefficients for  
999 soft X-rays by use of the electron microprobe. In: Newbury, D.E. (Eds.),  
1000 *Microbeam Analysis*. San Francisco, CA: San Francisco Press, pp. 319-324.

1001 Powell, R., Holland, T.J.B., 1994. Optimal geothermometry and geobarometry.  
1002 *American Mineralogist* 79, 120-133.

1003 Rapa, G., Groppo, C., Mosca, P., Rolfo, F., 2016. Petrological constraints on the  
1004 tectonic setting of the Kathmandu Nappe in the Langtang-Gosainkund-Helambu  
1005 regions, Central Nepal Himalaya. *Journal of Metamorphic Geology* 34, 999–1023.

1006 Rapa, G., Groppo, C., Rolfo, F., Petrelli, M., Mosca, P., Perugini, D., 2017. Titanite-  
1007 bearing calc-silicate rocks constrain timing, duration and magnitude of metamorphic  
1008 CO<sub>2</sub> degassing in the Himalayan belt. *Lithos* 292-293, 364-378.

1009 Reddy, S.M., Searle, M.P., Massey, J.A., 1993. Structural evolution of the High  
1010 Himalayan gneiss sequence, Langtang Valley, Nepal. In: Treloar, P.J., Searle,  
1011 M.P., (Eds.), *Himalayan Tectonics*. Geological Society of London Special  
1012 Publications 74, 375–389.

1013 Richards, A., Argles, T., Harris, N., Parrish, R., Ahmad, T., Darbyshire, F., Draganits,  
1014 E., 2005. Himalayan architecture constrained by isotopic tracers from clastic  
1015 sediments. *Earth and Planetary Science Letters* 236, 773–796.

- 1016 Robinson, D.M., DeCelles, P.G., Patchett, P.J., Garzione, C.N., 2001. The kinematic  
1017 evolution of the Nepalese Himalaya interpreted from Nd isotopes. *Earth and*  
1018 *Planetary Science Letters* 192, 507–521.
- 1019 Robinson, D.M., DeCelles, P.G., Copeland, P., 2006. Tectonic evolution of the  
1020 Himalayan thrust belt in western Nepal: implications for channel flow models.  
1021 *Geological Society of American Bulletin* 118, 865–885.
- 1022 Rolfo, F., Groppo, C., Mosca, P., 2015. Petrological constraints of the “Channel Flow”  
1023 model in eastern Nepal. In: Mukherjee, S., Carosi, R., van der Beek, P.A.,  
1024 Mukherjee, B.K., Robinson, D.M. (Eds.), *Tectonics of the Himalaya*. Geological  
1025 Society of London Special Publications 412, 177–197.
- 1026 Rubatto, D., Chakraborty, S., Dasgupta, S., 2013. Timescales of crustal melting in  
1027 the Higher Himalayan Crystallines (Sikkim, Eastern Himalaya) inferred from trace  
1028 element-constrained monazite and zircon chronology. *Contribution to Mineralogy*  
1029 *and Petrology* 165, 349-372.
- 1030 Searle, M.P., Law, R.D., Godin, L., Larson, K.P., Streule, M.J., Cottle, J.M., Jessup,  
1031 M.J., 2008. Defining the Himalayan Main Central Thrust in Nepal. *Journal of the*  
1032 *Geological Society of London* 165, 523–534.
- 1033 Schelling, D., 1992. The tectonostratigraphy and structure of the eastern Nepal  
1034 Himalaya. *Tectonics* 11, 925–943.
- 1035 Schelling, D., Arita, K., 1991. Thrust tectonics, crustal shortening, and the structure of  
1036 the far-eastern Nepal, Himalaya. *Tectonics* 10, 851–862.
- 1037 Stocklin, J., 1980. Geology of Nepal and its regional frame. *Journal of the Geological*  
1038 *Society of London* 137, 1-34.

- 1039 Tajčmanová, L., Connolly, J.A.D., Cesare, B., 2009. A thermodynamic model for  
1040 titanium and ferric iron solution in biotite. *Journal of Metamorphic Geology* 27,153–  
1041 165.
- 1042 Takagi, H., Arita, K., Sawaguchi, T., Kobayashi, K., Awaji, D., 2003. Kinematic history  
1043 of the Main Central Thrust zone in the Langtang area, Nepal. *Tectonophysics* 366,  
1044 151–163.
- 1045 Thompson, J.B., Hovis, G.L., 1979. Entropy of mixing in sanidine. *American*  
1046 *Mineralogist* 64, 57–65.
- 1047 Upreti, B. N., 1999. An overview of the stratigraphy and tectonics of the Nepal  
1048 Himalaya. *Journal of Asian Earth Sciences* 17, 577–606.
- 1049 Wang, J. M., Zhang, J. J., Wang, X.X., 2013. Structural kinematics, metamorphic P–  
1050 T profiles and zircon geochronology across the Greater Himalayan Crystalline  
1051 Complex in south-central Tibet: implication for a revised channel flow. *Journal of*  
1052 *Metamorphic Geology* 31, 607–628.
- 1053 Wang, J-M., Zhang, J-J., Liu, K., Wang, X-X., Rai, S., Scheltens, M., 2016. Spatial  
1054 and temporal evolution of tectonometamorphic discontinuities in the Central  
1055 Himalaya: Constraints from P-T paths and geochronology. *Tectonophysics* 679,  
1056 41-60.
- 1057 Waters, D.J., 2001. The significance of prograde and retrograde quartz-bearing  
1058 intergrowth microstructures in partially melted granulite-facies rocks. *Lithos* 56,  
1059 97–110.
- 1060 White, R.W., Powell, R., Holland, T.J.B., 2001. Calculation of partial melting equilibria  
1061 in the system Na<sub>2</sub>O-CaO-K<sub>2</sub>O-FeO-MgO-Al<sub>2</sub>O<sub>3</sub>-SiO<sub>2</sub>-H<sub>2</sub>O (NCKFMASH). *Journal*  
1062 *of Metamorphic Geology* 19, 139–153.

- 1063 White, R.W., Powell, R., Holland, T.J.B., 2007. Progress relating to calculation of  
1064 partial melting equilibria for metapelites. *Journal of Metamorphic Geology* 25, 511–  
1065 527.
- 1066 Whitney, D.L., Evans, B.W., 2010. Abbreviations for names of rock-forming minerals.  
1067 *American Mineralogist* 95, 185–187.
- 1068 Yakymchuk, C., Godin, L., 2012. Coupled role of deformation and metamorphism in  
1069 the construction of inverted metamorphic sequences: an example from far-  
1070 northwest Nepal. *Journal of Metamorphic Geology* 30, 513–535.
- 1071
- 1072

1073 **CAPTIONS**

1074 **Fig. 1** – Simplified geological map of central-eastern Himalaya, with major  
1075 tectonometamorphic units (modified from Goscombe and Hand, 2000, He et al.,  
1076 2015, Wang et al., 2016 and based on our own data). Traces for the three transects  
1077 studied in this paper are reported (G: Gatlang; L: Langtang; GH: Gosainkund-  
1078 Helambu). 1: Siwalik deposits; 2: Lesser Himalayan Sequence; 3: Lower Greater  
1079 Himalayan Sequence; 4: Upper Greater Himalayan Sequence; 5: Tethyan  
1080 Sedimentary Sequence (dark: Ordovician-Mesozoic; Light: Precambrian-Cambrian).  
1081 MFT: Main Frontal Thrust; MBT: Main Boundary Thrust; MCT: Main Central Thrust;  
1082 STDS: South Tibetan Detachment System. The study area is located in the white  
1083 rectangle, and reported in Fig. 2.

1084

1085 **Fig. 2** – Geological map of the investigated area, with equal area stereo plots of  
1086 representative structural data. LT, Langtang Thrust; MCT, Main Central Thrust; RT,  
1087 Ramgarh Thrust; LHS, Lesser Himalayan Sequence; L-GHS, Lower Greater  
1088 Himalayan Sequence; U-GHS, Upper Greater Himalayan Sequence.

1089

1090 **Fig. 3** – Representative LHS and LHS-Ramgarh Thrust Sheet lithologies at the  
1091 meso- and microscale. (a,b) Graphite-rich two-mica phyllite with porphyroblastic  
1092 garnet from the LHS. Garnet is partially wrapped around by the  $S_{2(LHS)}$  foliation  
1093 defined by the alignment of Bt + Wm + Gr; its rim, however, overgrows the  $S_{2(LHS)}$   
1094 foliation. Note the rotated internal schistosity in Grt (b: Plane Polarized Light, PPL).  
1095 (c,d) Quartzites from the LHS-Ramgarh Thrust Sheet. In (c), quartzites (bottom) are  
1096 in contact with phyllitic schists (top). Quartzites are strongly foliated, with the main  
1097  $S_{2(L-GHS)}$  foliation defined by Bt + Wm + St alignment (d: PPL). (e, f) Two-mica augen

1098 gneiss from the LHS-Ramgarh Thrust Sheet, showing a well-developed mylonitic  
1099 fabric defined by Wm + Bt. (f: Crossed Polarized Light, XPL).

1100

1101 **Fig. 4** –Representative meso- and micro-structures of the LHS and LHS-Ramgarh  
1102 Thrust Sheet lithologies. (a) Mesoscopic shear zones developed during the  $D_{2(LHS)}$   
1103 phase, leading to the progressive parallelization of the  $S_{1(LHS)}$  and  $S_{2(LHS)}$  foliations.  
1104 (b) Mica-fish showing top-to-the-south sense of shear. (c)  $S_{2(LHS)}$  foliation folded and  
1105 crenulated by  $D_{3(LHS)}$  phase. (d) Mesoscopic relationships between the  $L_{2(LHS)}$  and  
1106  $L_{cr3(LHS)}$ . (e,f) Late top-to-the-north extensional structures in the LHS lithologies.

1107

1108 **Fig. 5** – Representative Lower-GHS (L-GHS) lithologies at the meso- and microscale.  
1109 (a) Compositional layering in two-micas + Grt metapelites, with bands parallel to the  
1110  $S_{2(L-GHS)}$  schistosity. (b) Kyanite porphyroblasts are elongated parallel to the  $S_{2(L-GHS)}$   
1111 and define a stretching lineation.  $S_{2(L-GHS)}$  schistosity is indicated. (c) Layers of  
1112 micaschists with variable thickness intercalated in fine-grained gneisses. (d) Detail of  
1113 a melt-related microstructure (melt pseudomorph) in a Lower-GHS sample from the  
1114 uppermost structural levels (PPL). (e) Boudin of a Cpx + Pl ± Grt ± Scp ± Kfs ± Cal  
1115 calc-silicate rock, outcropping in the Helambu region. (f) Banded quartzites from the  
1116 lowermost structural levels of the Lower-GHS (Gatlang region).

1117

1118 **Fig. 6** – Representative mesostructures of Lower-GHS (L-GHS) lithologies. (a)  
1119 Relationships between  $S_{2(L-GHS)}$  and  $S_{3(L-GHS)}$  schistositities. (b-d) Deformation  
1120 structures related to the  $D_{3(L-GHS)}$  event, leading to pervasive stretching and  
1121 boudinage.

1122



1123 **Fig. 7** – Representative lithologies and mesostructures of Upper-GHS (U-GHS). (a)  
1124 Migmatitic paragneiss with leucosomes parallel to the  $S_{m(U-GHS)}$ . (b) Detail of a Grt +  
1125 Sil gneiss, with garnet porphyroblasts surrounded by a plagioclase corona. (d) Layers  
1126 of calc-silicate rocks (Cpx + Kfs + Scp  $\pm$  Pl  $\pm$  Qz  $\pm$  Cal), variably deformed. (d) Metre  
1127 thick layer of fine-grained biotitic gneiss with Sil-rich nodules, intercalated within  
1128 migmatitic orthogneisses. (e) Strongly mylonitic migmatitic paragneiss in the Gatlang  
1129 region, with leucosomes elongated parallel to the main foliation. (f) Shear zone with  
1130 top-to-the-south movement in the mylonitic migmatitic gneisses.

1131

1132 **Fig. 8** – Representative microstructures of the studied samples. (a) Sample 15-19.  
1133 The main  $S_{2(LHS)}$  foliation is defined by Bt + Wm, while skeletal Grt preserves an  
1134 internal rotated foliation (inset). (PPL, inset: XPL). (b,c) Sample 15-28b.  
1135 Porphyroblastic Grt has an internal foliation which is continuous with the external  
1136  $S_{2(LHS)}$  foliation, defined by Wm + Bt (PPL). Ky occur as inclusions in Grt rims (b) and  
1137 in the matrix (c), and St is included in Grt rim (c). The inset in (c) shows  $S_{1(LHS)}$   
1138 preserved in a microlithon (PPL). (d,e) Sample 15-26b. Grt porphyroblasts are partly  
1139 wrapped by the  $S_{2(LHS)}$  foliation, and Grt rims show straight equilibrium contacts with  
1140 both Bt and Wm. The inset shows the  $S_{2(LHS)}$  foliation defined by Bt + Wm. (e). Grt  
1141 includes Qz, Bt, Wm, Rt, Ilm and Pl (not shown) (d: PPL, inset: XPL; e: BSE). (f,g)  
1142 Sample 15-38. Large Grt porphyroblasts (bottom left) are partly wrapped by the main  
1143  $S_{2(L-GHS)}$  foliation, defined by Bt + Wm alignment (inset) (PPL, inset: XPL). In (g) St in  
1144 the matrix includes Rt, Qz and Pl and Ky is replaced by Wm (PPL). (h,i) Sample 14-  
1145 12. In (h) the compositional banding is defined by Bt + Sil mesocratic domains,  
1146 alternating with Qz + Pl + Kfs  $\pm$  Bt leucocratic domains (PPL). Wm locally replaces  
1147 Sil. In (i) skeletal Grt is replaced by a Pl corona, and includes Bt, Pl and Qz (XPL).

1148

1149 **Fig. 9** – P-T conditions obtained using the Average PT approach applied to LHS and  
1150 GHS metapelite samples. (a, b) LHS samples: prograde and peak P-T conditions  
1151 with uncertainties (a) and P-T evolutions inferred basing on AvPT results (arrows, b).  
1152 (c, d) GHS samples from the Gatlang-Langtang transects: prograde and peak P-T  
1153 conditions with uncertainties (c) and P-T evolutions inferred basing on AvPT results  
1154 (arrows, d). (e, f) GHS samples from the Gosainkund-Helambu transect: peak P-T  
1155 conditions with uncertainties. Light grey and dark grey fields are the Wm and Bt  
1156 dehydration melting fields respectively, separated by the H<sub>2</sub>O-saturated *solidus* and  
1157 the Wm–out reaction (modified from White et al., 2001).

1158

1159 **Fig. 10** – (a, b) Estimated peak temperature (a) and pressure (b) conditions, reported  
1160 from left to right from lower to upper structural levels. The x-axis is not to scale. T and  
1161 P results constrained using the Average PT method (circles) are compared to results  
1162 obtained using pseudosections (squares) (derived from Rapa et al., 2016, except for  
1163 sample 15-26b which has been modelled in this study). The lines (and coloured  
1164 boxes) refer to the weighted mean values (and errors) obtained with the  
1165 pseudosection approach; the **dashed** lines (and dashed boxes) refer to the weighted  
1166 mean values (and errors) obtained with the Average PT method; **the dotted lines**  
1167 **(and dotted boxes) refer to the weighted mean values (and errors) obtained for the**  
1168 **Kohn (2008) samples, calculated using the conventional thermobarometry approach.**  
1169 (c) T/P ratios (°C/kbar) (with errors) plotted as a function of the (approximate)  
1170 structural position for the samples studied in this work (sample 15-26b) and in Rapa  
1171 et al. (2016). The lines (and coloured boxes) refer to the weighted mean values (and  
1172 errors) obtained with the pseudosection approach; the **dashed** lines (and dashed

1173 boxes) refer to the weighted mean values (and errors) obtained with the Average PT  
1174 method; the dotted lines (and dotted boxes) refer to the weighted mean values (and  
1175 errors) obtained for the Kohn (2008) samples, calculated using the conventional  
1176 thermobarometry approach.

1177

1178 **Fig. 11** –  $P$ - $T$  pseudosection for sample 15-26b (LHS-Ramgarh Thrust Sheet,  
1179 Gatlang transect) calculated in the MnNCKFMASH system at  $a(\text{H}_2\text{O})=1$ .  
1180 Unfractionated and fractionated (\*) bulk-rock compositions are given in mol%. (a)  $P$ -  
1181  $T$  pseudosection calculated using the unfractionated bulk composition, used to model  
1182 the  $P$ - $T$  conditions for the growth of Grt core. In (a-c), di-, tri-, quadri-, quini-, esa-  
1183 and epta- variant fields are represented in different grey tones, from white (di-  
1184 variant) to the darker grey (epta-variant). Ms and Pg refer to K-rich and Na-rich  
1185 white micas, respectively. The white dotted rectangle in (a) refers to the  $P$ - $T$  interval  
1186 shown in (b), (c) and (d). (b) Detail of (a) with compositional isopleths of Grt core. (c)  
1187  $P$ - $T$  pseudosection calculated using the fractionated bulk composition, used to model  
1188 the  $P$ - $T$  conditions for the growth of Grt rim, contoured for Grt rim composition. The  
1189 white dashed polygon in (b) and (c) constrain the  $P$ - $T$  conditions inferred for the  
1190 growth of Grt core and rim, respectively. (d)  $P$ - $T$  path inferred for sample 15-26b  
1191 basing on mineral assemblages and compositions (light purple arrow). The dashed  
1192 lines (melt-in) in (a) to (d) are the  $\text{H}_2\text{O}$ -saturated solidus.

1193

1194 **Fig. 12** –  $P$ - $T$  diagrams showing the  $P$ - $T$  trajectories obtained for the studied  
1195 metapelites from the Gatlang-Langtang (a,c) and Gosainkund-Helambu (b,d)  
1196 transects using the pseudosection (a,b) and AvPT (c,d) approaches (Rapa et al.,  
1197 2016 and this study). Asterisks in (a,b) indicate data from Rapa et al. (2016). Light

1198 grey and dark grey fields represent Wm and Bt dehydration melting fields,  
1199 respectively, separated by the H<sub>2</sub>O-saturated solidus and the Wm-out reaction  
1200 (modified from White et al., 2001).

Figure 1  
[Click here to download high resolution image](#)

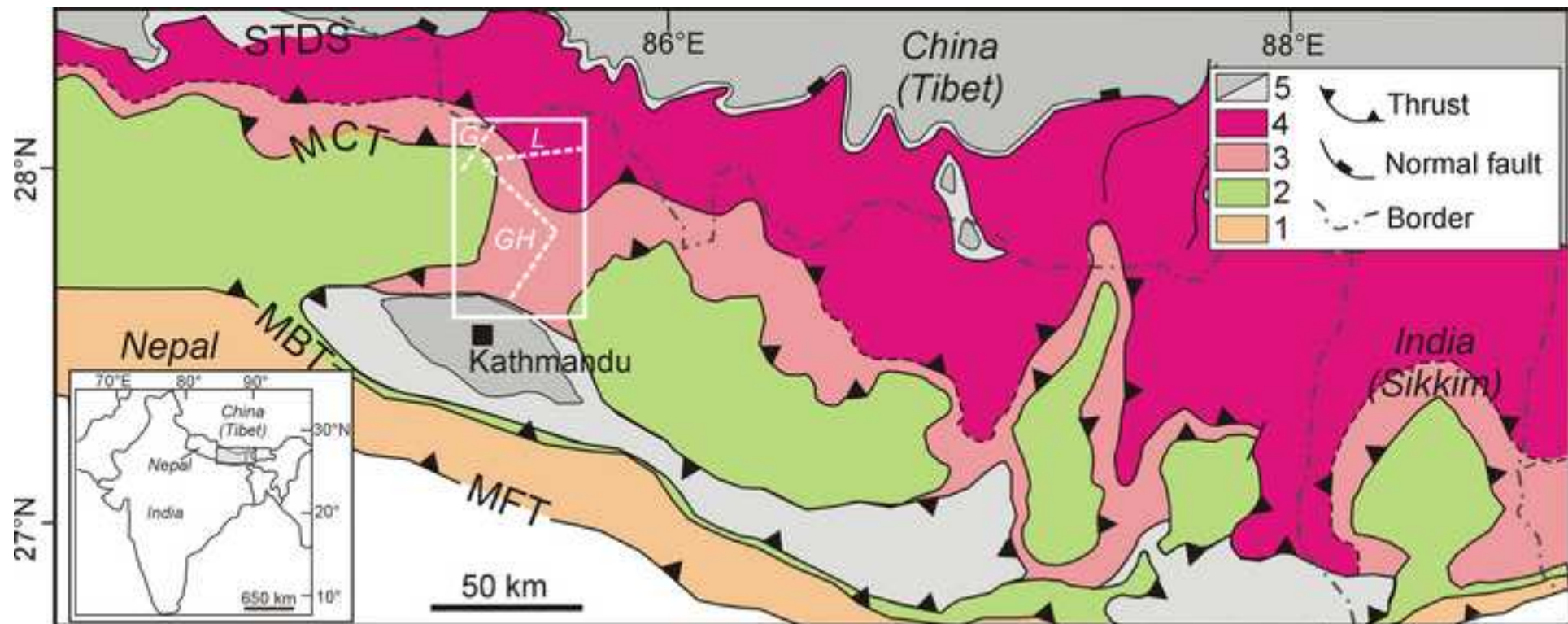


Figure 2  
[Click here to download high resolution image](#)

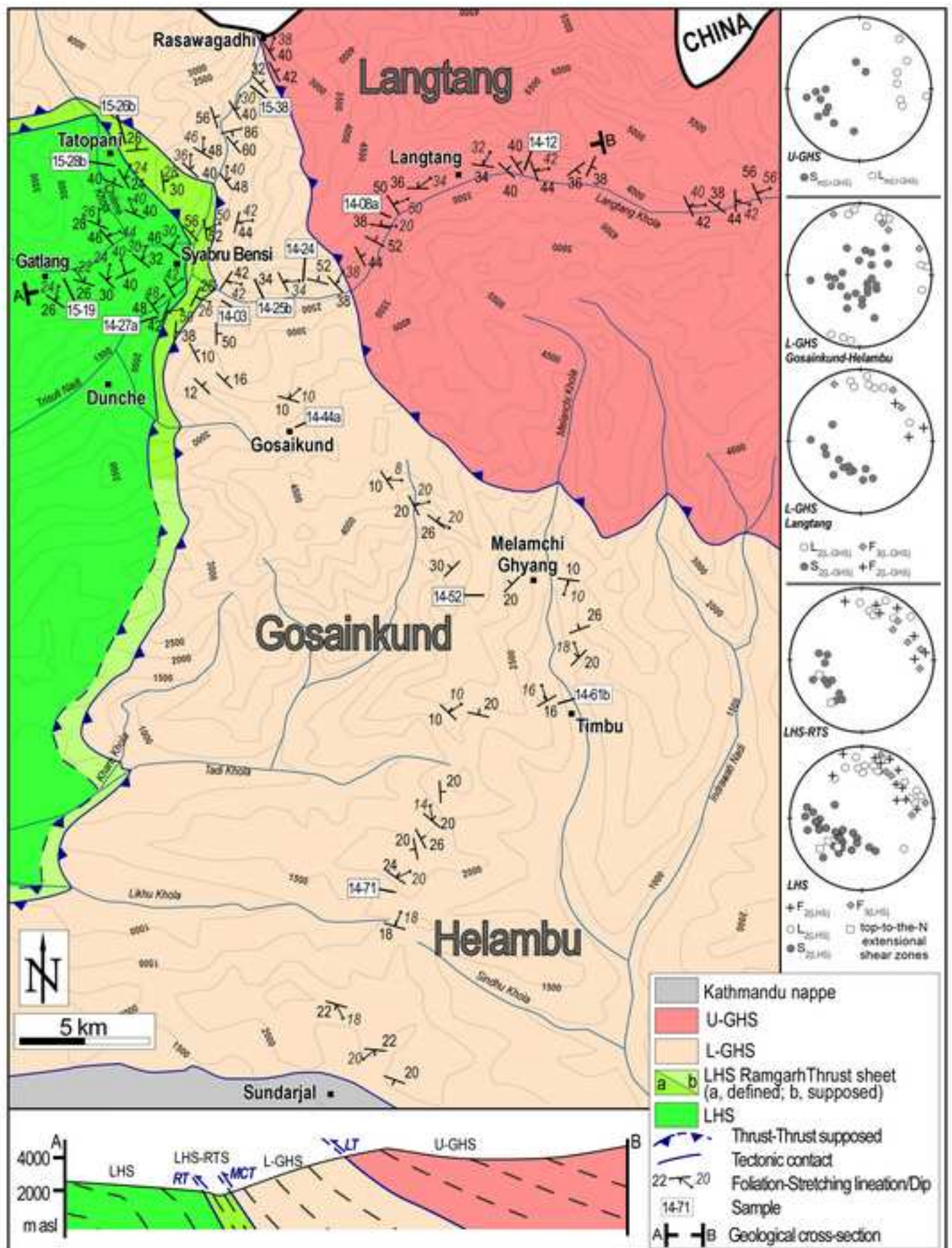


Figure 3  
[Click here to download high resolution image](#)

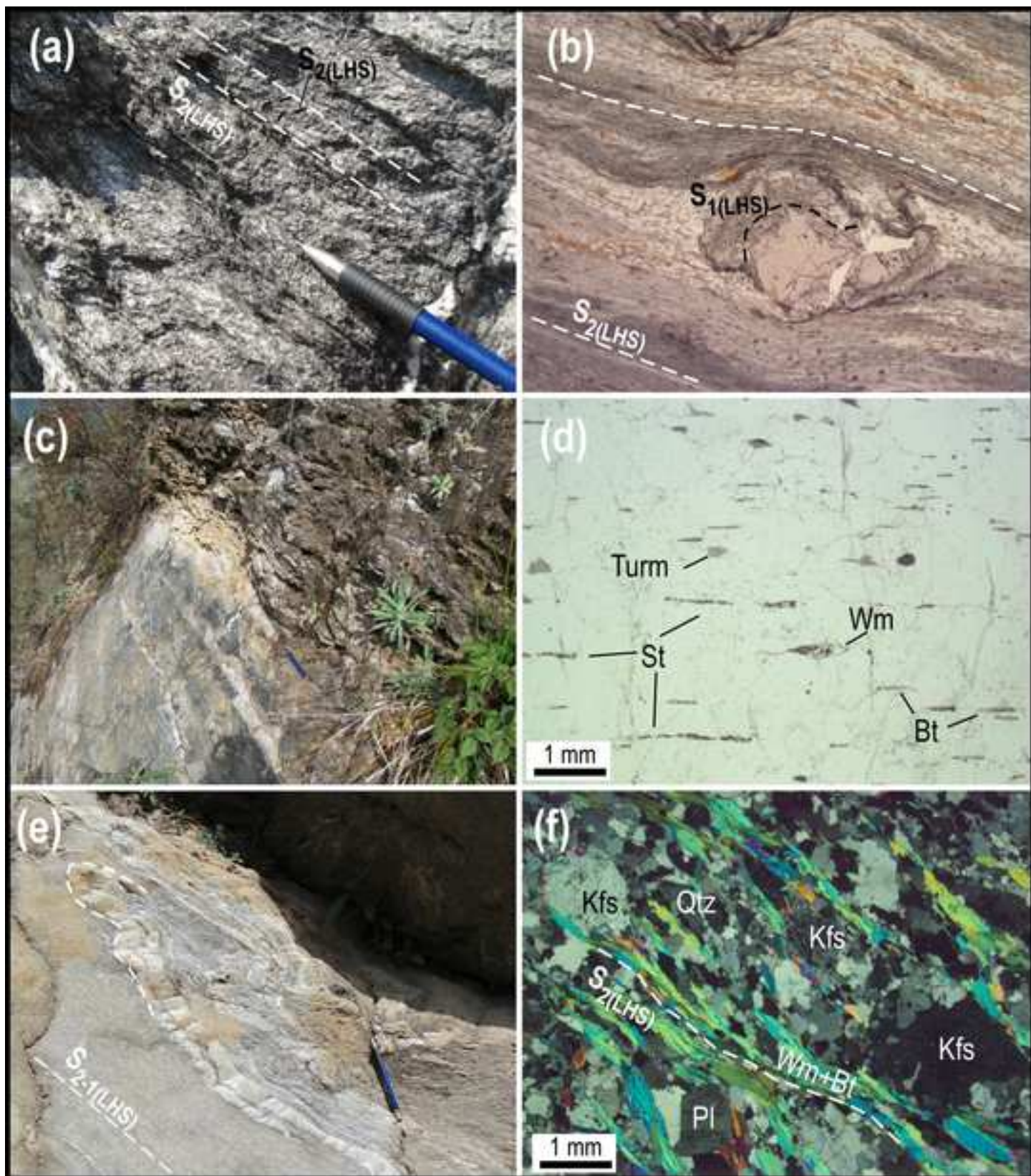


Figure 4  
[Click here to download high resolution image](#)

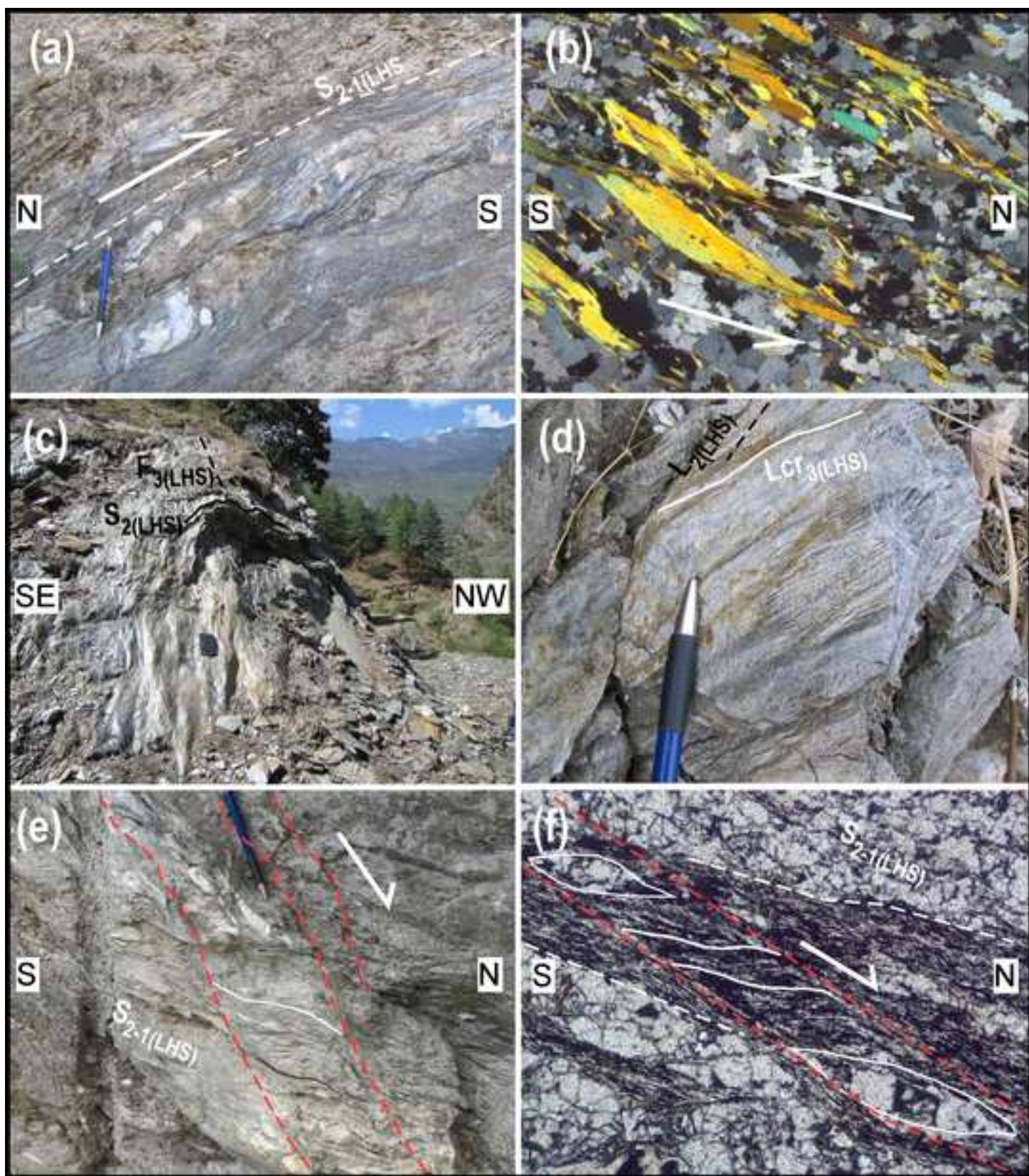




Figure 5  
[Click here to download high resolution image](#)

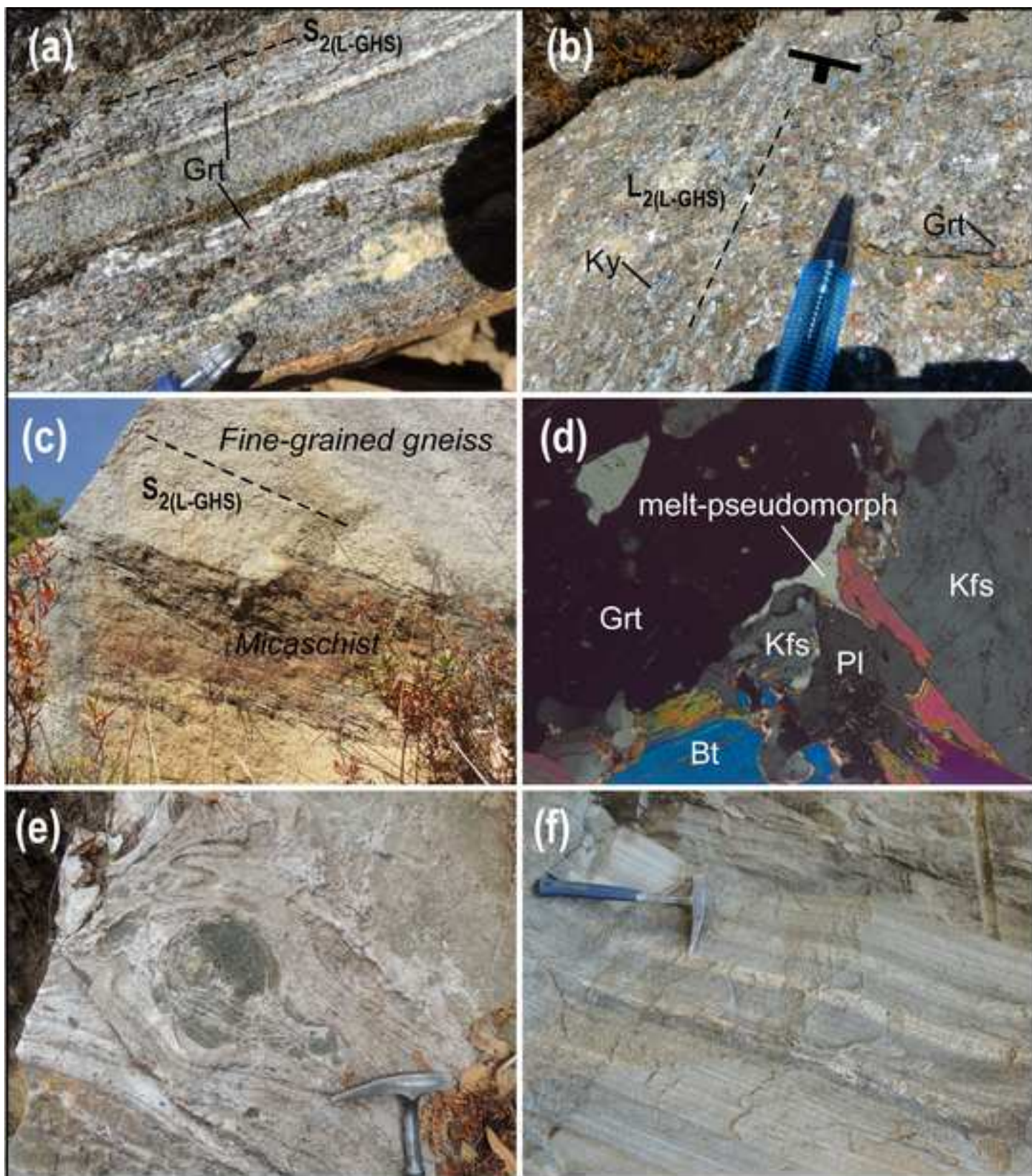


Figure 6  
[Click here to download high resolution image](#)

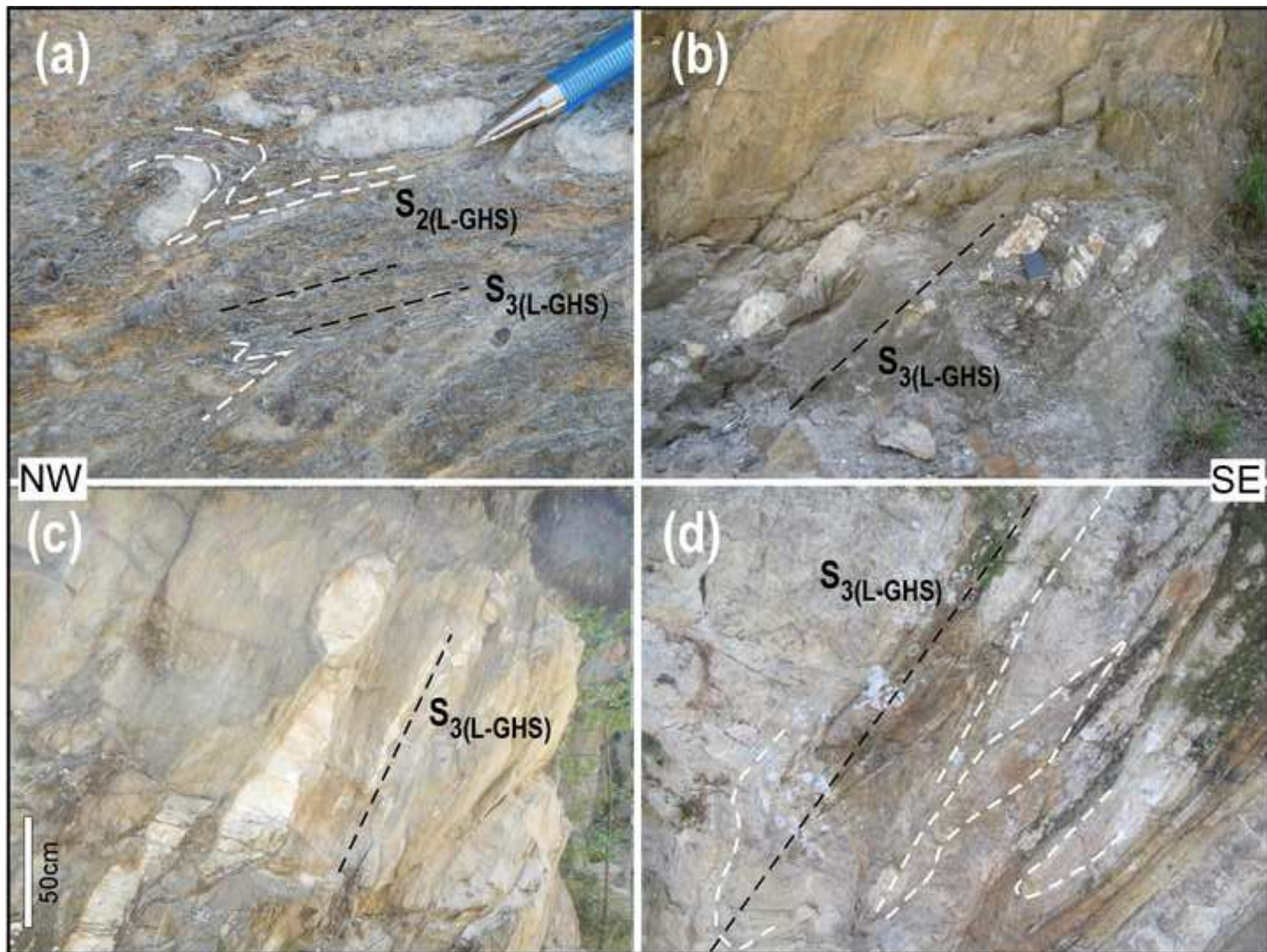


Figure 7  
[Click here to download high resolution image](#)

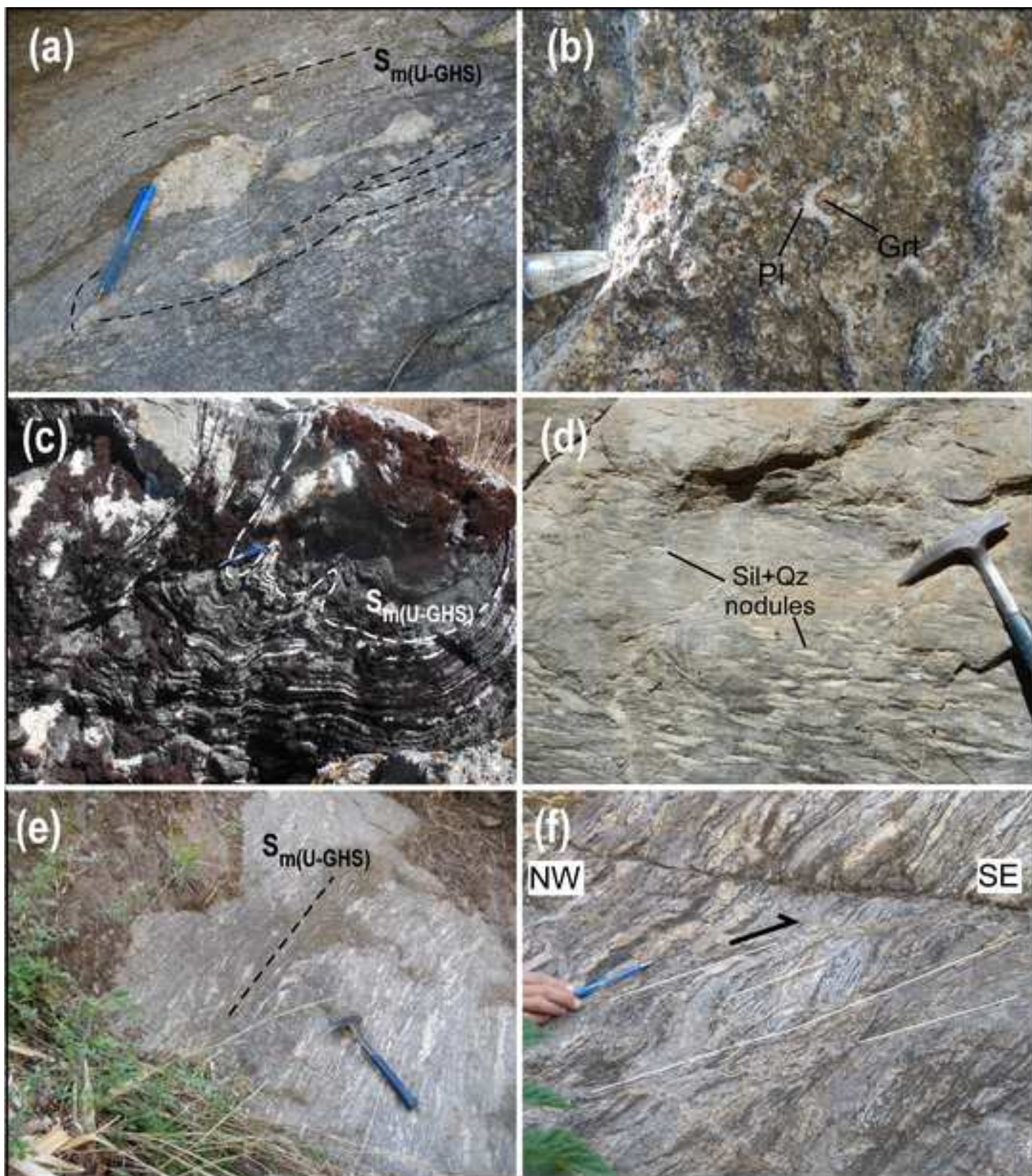


Figure 8  
[Click here to download high resolution image](#)

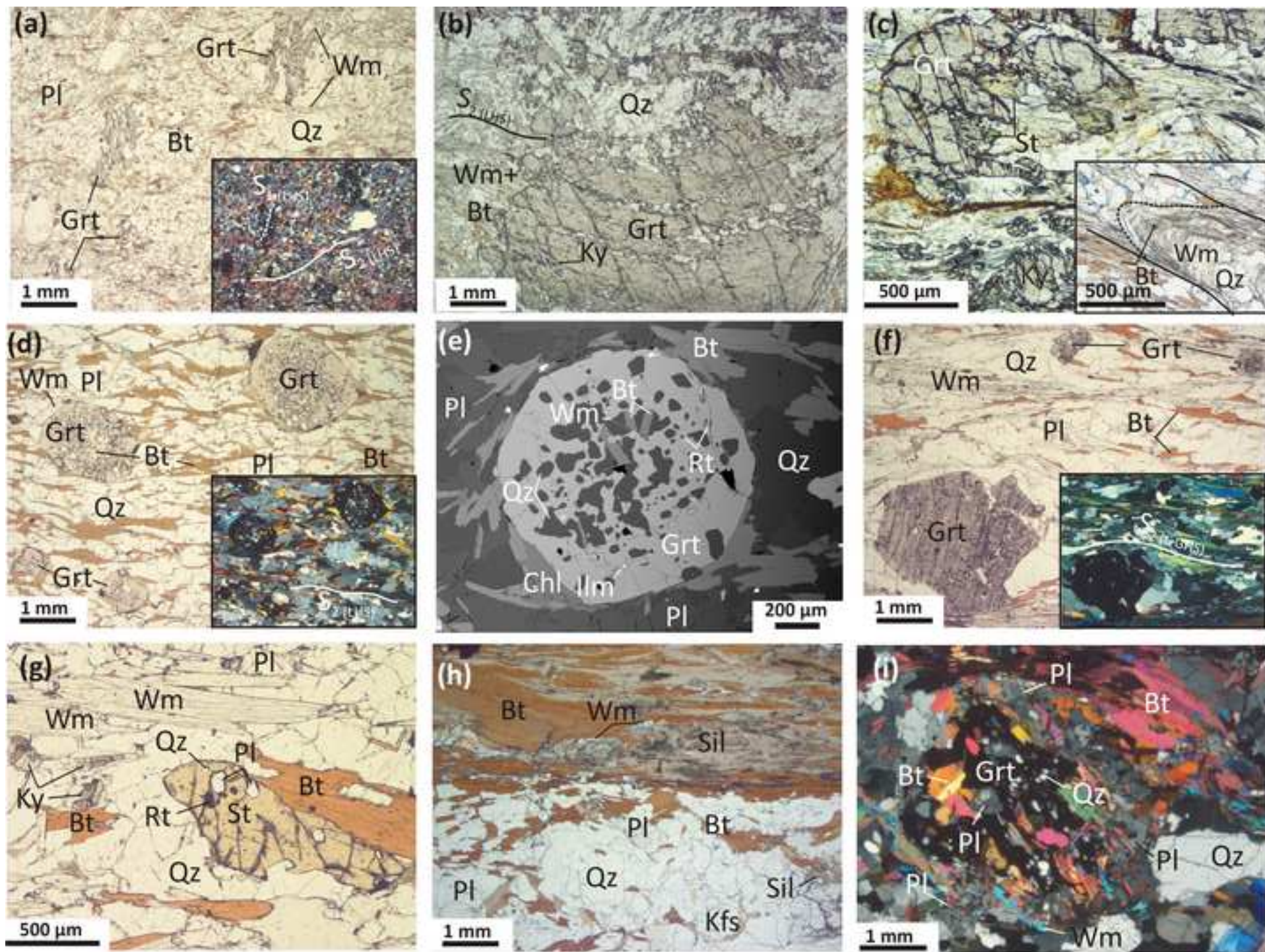


Figure 9  
[Click here to download high resolution image](#)

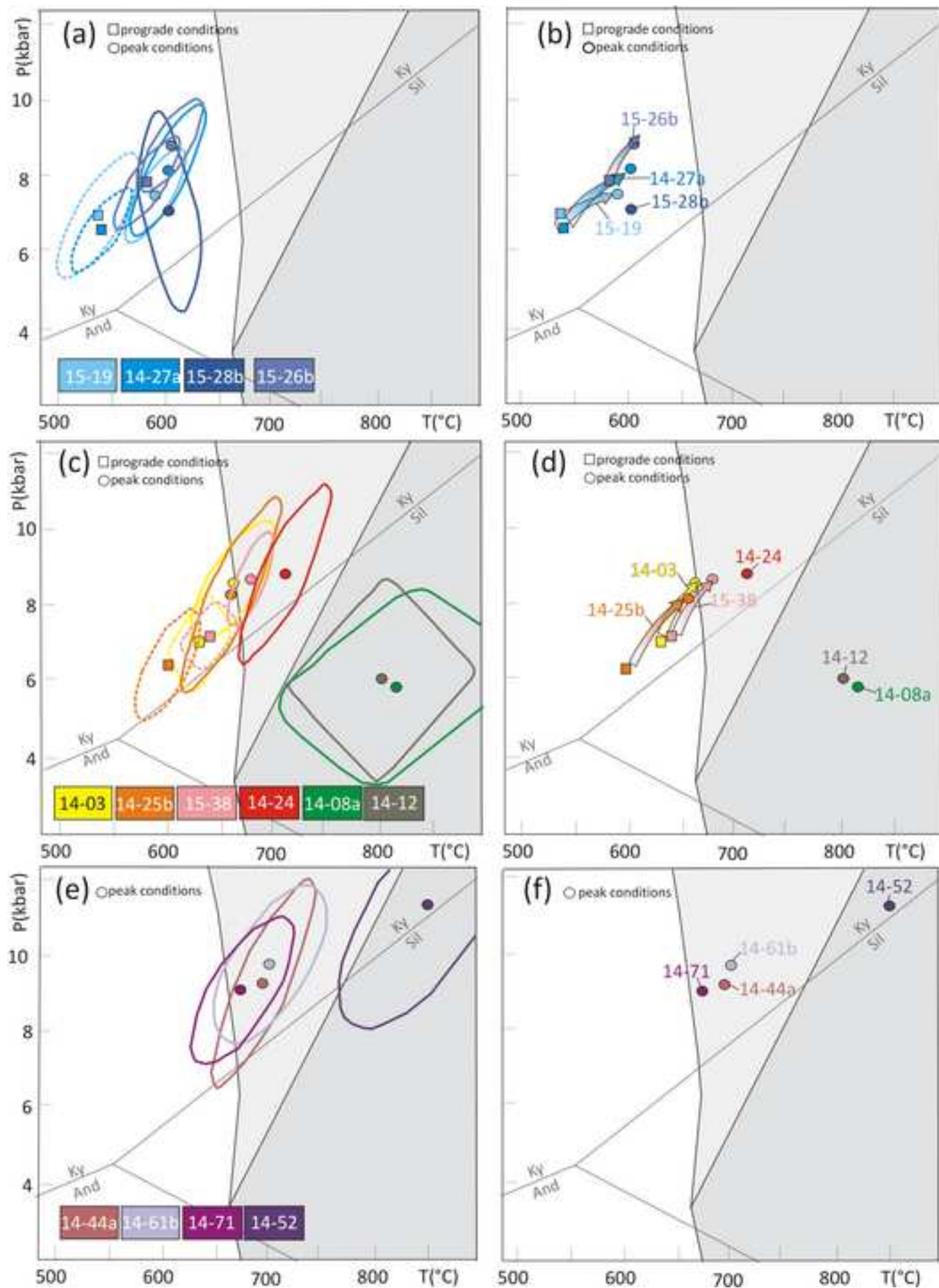


Figure 10

[Click here to download high resolution image](#)

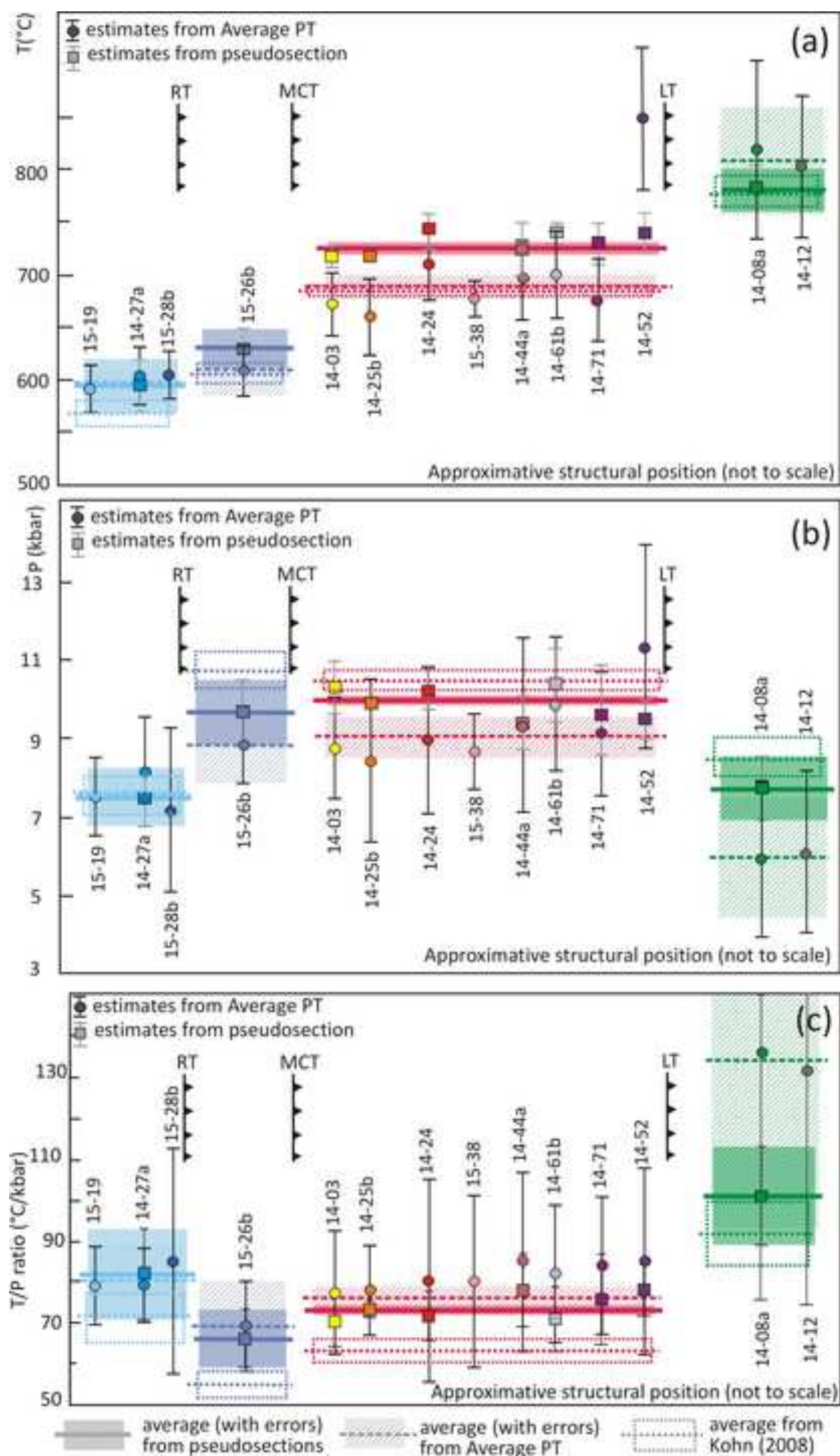


Figure 11

[Click here to download high resolution image](#)

SiO<sub>2</sub>(72.26)Al<sub>2</sub>O<sub>3</sub>(9.17)FeO(5.82)MgO(4.71)MnO(0.17)CaO(2.49)Na<sub>2</sub>O(2.99)K<sub>2</sub>O(1.74)TiO<sub>2</sub>(0.68)

\*SiO<sub>2</sub>(73.02)Al<sub>2</sub>O<sub>3</sub>(9.04)FeO(5.25)MgO(4.72)MnO(0.07)CaO(2.36)Na<sub>2</sub>O(3.07)K<sub>2</sub>O(1.79)TiO<sub>2</sub>(0.69)

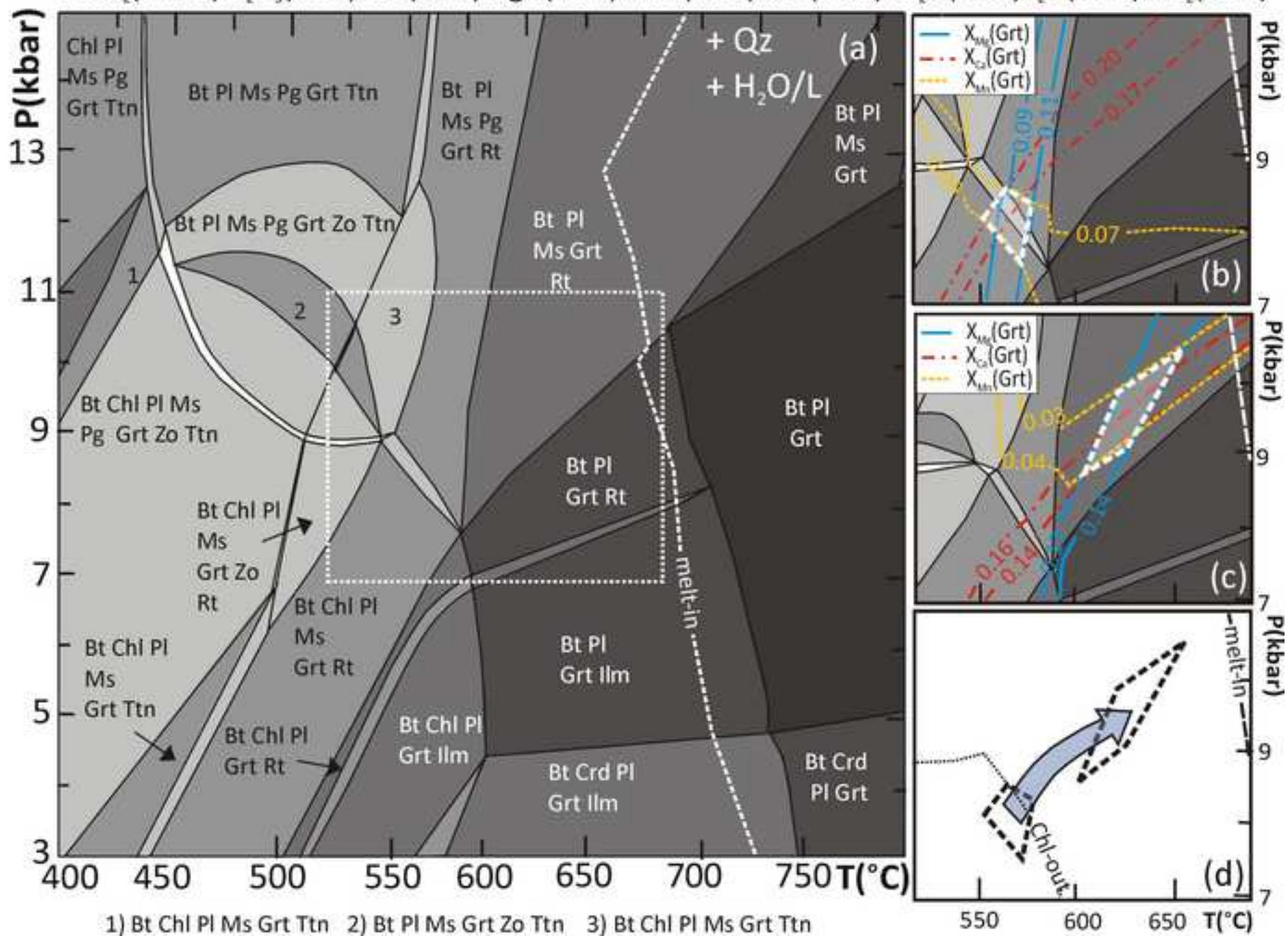


Figure 12

[Click here to download high resolution image](#)

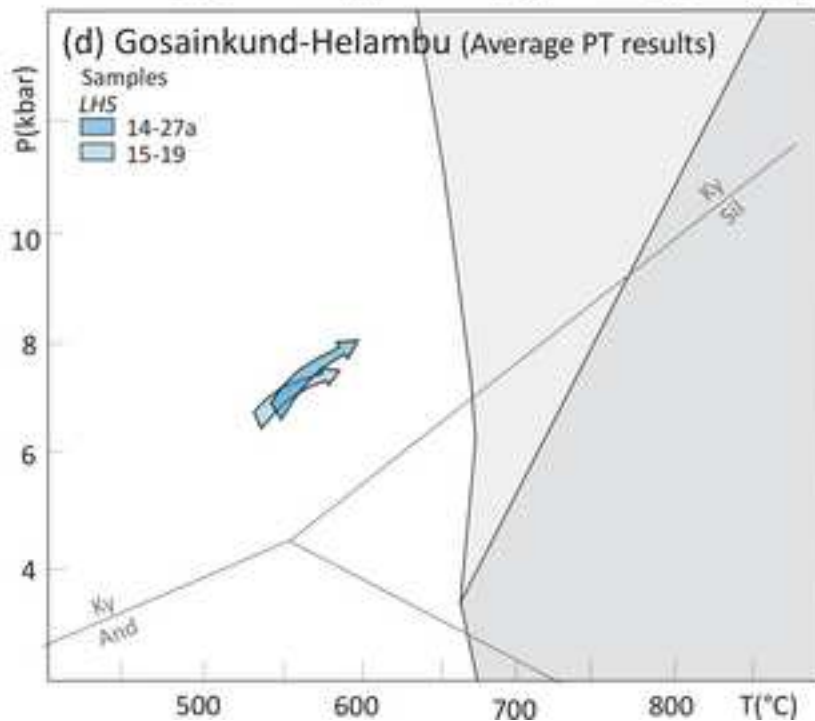
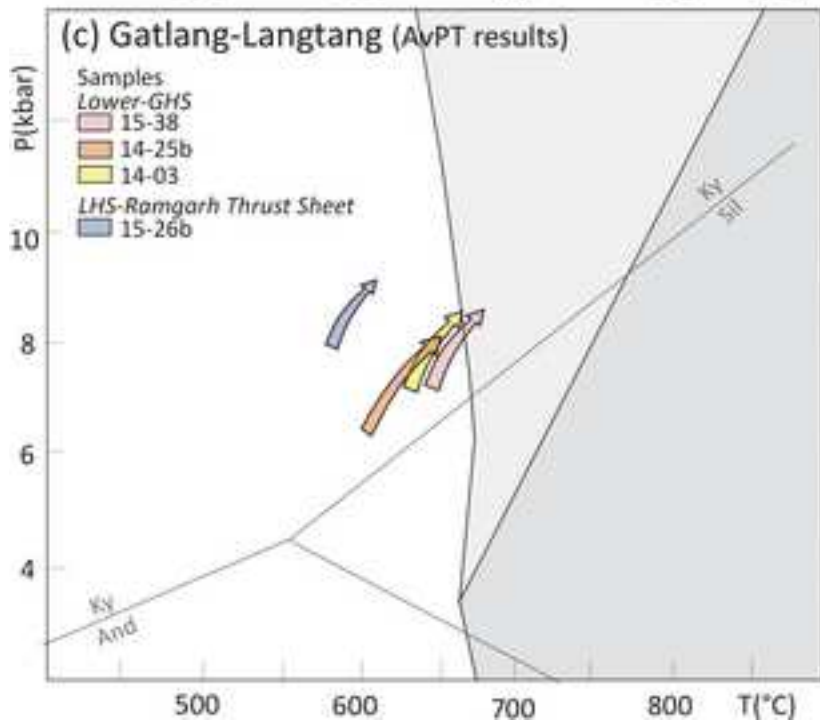
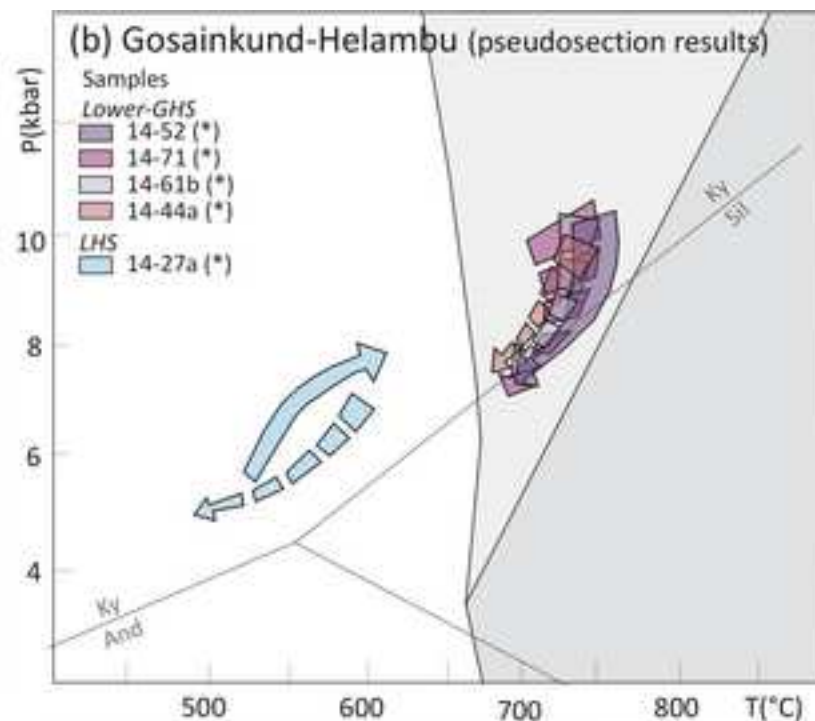
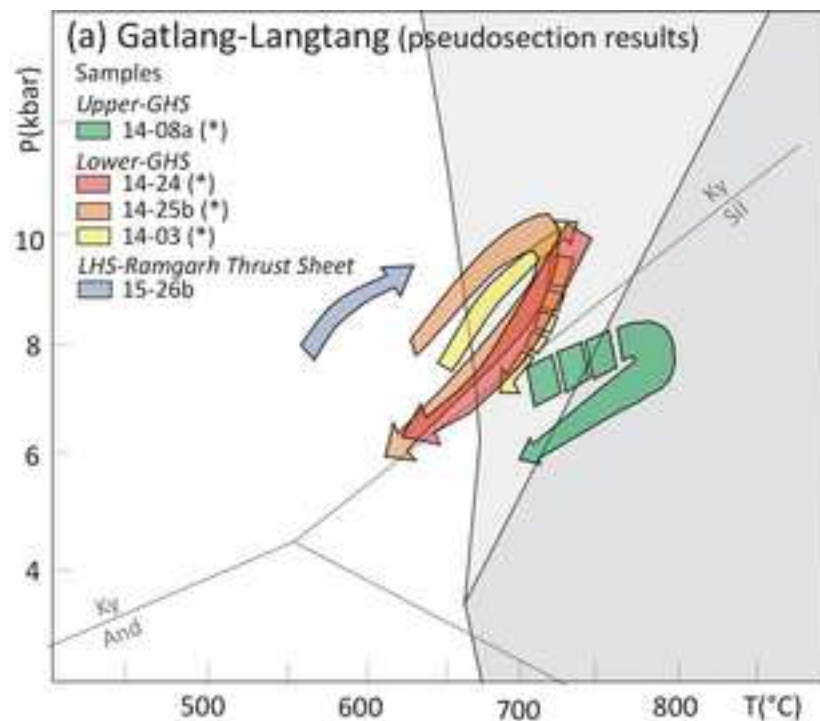




Table 1

Table 1 - Microstructural features of metapelites from Rapa et al. (2016)

	Sample	Main assemblage	Accessories	Comments	
LHS	14-27a	Two-mica graphitic phyllite, with porphyroblastic Grt	Qz, Pl, Wm, Bt, Chl, Grt	Ep, Gr, Tur, Op	$S_{1(LHS)}$ : Chl + Bt + Wm + Pl + Ilm; $S_{2(LHS)}$ : Bt + Wm + Gr. Grt is partly wrapped by $S_{2(LHS)}$ and includes rotated internal foliation defined by Qz + Chl + Ilm + Gr. Late Bt, Chl and Wm overgrow $S_{2(LHS)}$ .
	14-03	Wm + Bt + Grt micaschist	Qz, Pl, Wm, Bt, Grt, <<Sil	Rt, Ilm, Tur	$S_{2(L-GHS)}$ : Wm + Bt. Grt core is crowded with inclusions (Qz + Bt + Chl + Rt + Ilm), whereas Grt rim is inclusion-free. Transition from Grt core to Grt rim is marked by nanogranites. Sil occurs at Grt and Wm rims.
	14-25b	Wm + Bt + Grt + Ky + St micaschist	Qz, Pl, Wm, Bt, Grt, Ky, St, <<Sil	Rt, Ilm, Tur	$S_{2(L-GHS)}$ : Wm + Bt. Grt core is crowded with inclusions (Qz + Bt + Ilm), whereas Grt rim is inclusion-free. Transition from Grt core to Grt rim is marked by nanogranites. Ky is either in equilibrium with $S_{2(L-GHS)}$ or overgrows it. St overgrow $S_{2(L-GHS)}$ and replaces Ky. Sil occurs at Grt rims. Wm flakes overgrows $S_{2(L-GHS)}$ .
L-GHS	14-24	Wm + Bt + Grt + Ky gneissic micaschist	Qz, Pl, Wm, Bt, Grt, Ky, St, <<Sil	Rt, Ilm, Tur	$S_{2(L-GHS)}$ : Wm + Bt. Grt core is crowded with inclusions (Qz + Bt + Pl + Wm + Rt + Ilm), whereas Grt rim is inclusion-free. Transition from Grt core to Grt rim is marked by nanogranites. Ky is either in equilibrium with $S_{2(L-GHS)}$ or overgrows it. Sil occurs at Grt rims. Wm flakes overgrow $S_{2(L-GHS)}$ .
	14-44a	Wm + Bt + Ky micaschist, with porphyroblastic Grt	Qz, Pl, Bt, Wm, Grt, Ky	Rt, Ilm, Gr	$S_{2(L-GHS)}$ : Wm + Bt + Gr. Grt core is crowded with inclusions, Grt rim is inclusion-free. Transition from Grt core to Grt rim is marked by nanogranites. Ky is rare. Wm flakes overgrow $S_{2(L-GHS)}$ .
	14-61b	Bt + Wm micaschist, with porphyroblastic Grt	Qz, Pl, Kfs, Bt, Wm, Grt	Ilm	$S_{2(L-GHS)}$ : Bt + <Wm. Grt porphyroblasts are wrapped by it; they include Qz + Bt + Wm + Ilm. Grt is locally peritectic and includes Wm + Pl + Qz. Kfs is replaced by Pl. Pl is locally anti-perthitic. Wm flakes overgrows $S_{2(L-GHS)}$ .
	14-71	Bt + Wm + Grt + Sil gneissic micaschist	Qz, Pl, Bt, Wm, Grt, Sil	Ilm	$S_{2(L-GHS)}$ : Bt + Wm. Grt core is crowded with inclusions (Qz + Pl + Bt Ilm), whereas Grt rim is inclusion-free. Transition from Grt core to Grt rim is marked by nanogranites. Late Wm flakes overgrow $S_{2(L-GHS)}$ and include Sil. Wm flakes overgrow $S_{2(L-GHS)}$ .
	14-52	Bt + Sil + Ky fine-grained gneiss, with porphyroblastic Grt	Qz, Pl, Bt, <<Wm, Grt, Sil, <Ky	Ilm	Banded structure, defined by Qz + Bt + Pl ± Ky ± Grt ± Sil mesocratic domains, alternated with Sil + Qz ± Pl ± Bt leucocratic layers; $S_{2(L-GHS)}$ is defined by Bt + Sil. Grt is rare and includes Qz + Bt + Wm + Ky at its rims. Ky in the matrix is replaced by Pl.
U-GHS	14-08a	Bt + Sil + Grt migmatite	Qz, Pl, Bt, Wm, Kfs, Grt, Sil	Ilm	Banded structure, defined by Bt + Sil + Qz ± Grt mm-thick mesocratic domains alternating with Qz + Pl + Kfs ± Sil ± Grt pluri-mm leucocratic layers; $S_{m(U-GHS)}$ defined by Bt + Sil. Grt is peritectic with nanogranites. Mirmeckites and symplectites are common. Local occurrence of melt pseudomorphs. Wm flakes overgrow $S_{m(U-GHS)}$ .



Table 2

Table 2. Mineral compositions for the studied metapelites

	Grt	Bt	Wm	Pl	St	Chl
LHS	→		→			
		XMg <sup>i</sup> =0.39 Ti <sup>i</sup> =0.03	Si <sup>#</sup> =3.09-3.10 Na <sup>#</sup> =0.12-0.20			
	XMg=0.03-0.07 XCa=0.19-0.09 XMn=0.16-0.02 XFe=0.63-0.81	XMg <sup>#</sup> =0.39-0.41 Ti <sup>#</sup> =0.10-0.11	Si=3.09-3.18 Na=0.14-0.20	XAn=0.21-0.23 XAn <sup>i</sup> =0.18-0.22		XMg <sup>*</sup> =0.39-0.40
LHS	→			→		
	XMg=0.030-0.055 XCa=0.25-0.19 XMn=0.15-0.05 XFe=0.57-0.72	XMg=0.38-0.43 Ti=0.09-0.13	Si <sup>#</sup> =3.05-3.13 Na <sup>#</sup> =0.08-0.14	XAn=0.34-0.28		XMg <sup>i</sup> =0.39 XMg <sup>#</sup> =0.41-0.44 XMg <sup>*</sup> =0.41-0.44
			Si=3.05-3.17 Na=0.08-0.14			
LHS (RTS)	→				→	
	XMg=0.08-0.13 XCa=0.17-0.14 XMn=0.02-0.00 XFe=0.72-0.75	XMg=0.51-0.56 Ti=0.06-0.10	Si=3.08-3.20 Na=0.1-0.14		XMg=0.18-0.13	
LHS (RTS)	→			→		
	XMg=0.09-0.14 XCa=0.2-0.14 XMn=0.09-0.03 XFe=0.64-0.70	XMg <sup>i</sup> =0.57-0.59 Ti <sup>i</sup> =0.09-0.10	Si=3.07-3.18 Na=0.15-0.19	XAn=0.30-0.24		XMg <sup>*</sup> =0.16
		XMg=0.50-0.52 Ti=0.10-0.13				
L-GHS	→			→		
	XMg=0.14-0.18 XCa=0.075-0.05 XMn=0.07-0.035 XFe=0.71-0.74	XMg <sup>i</sup> =0.61-0.68 Ti <sup>i</sup> =0.09-0.12	Si=3.09-3.14 Na=0.13-0.14	XAn=0.17-0.22		XMg <sup>*</sup> =0.24-0.51
		XMg=0.44-0.51 Ti=0.10-0.18				
	→			→		
XMg=0.13-0.15 XCa=0.04-0.03 XMn=0.05-0.035 XFe=0.78-0.81	XMg <sup>i</sup> =0.44-0.54 Ti <sup>i</sup> =0.10-0.14	Si=3.07-3.10 Na=0.15-0.17	XAn <sup>i</sup> =0.12 XAn=0.15-0.16	XMg=0.16-0.12		
	XMg=0.38-0.46 Ti=0.09-0.17					
L-GHS	→				→	
	XMg=0.09-0.14 XCa=0.08-0.04 XMn=0.11-0.03 XFe=0.72-0.80	XMg <sup>i</sup> =0.51 Ti <sup>i</sup> =0-0.11	Si <sup>*</sup> =3.03-3.09 Na <sup>*</sup> =0.15-0.22	XAn <sup>i</sup> =0.30-0.32 XAn=0.16-0.24	XMg=0.20-0.16	XMg <sup>*</sup> =0.26-0.36
		XMg=0.48-0.50 Ti=0.09-0.17	Si=3.08-3.16 Na=0.15-0.22			
L-GHS	→			→	→	
	XMg=0.14-0.16 XCa=0.05-0.04 XMn=0.05-0.04 XFe=0.75-0.79	XMg <sup>i</sup> =0.50-0.55 Ti <sup>i</sup> =0.13-0.16	Si=3.08-3.15 Na=0.13-0.14	XAn <sup>i</sup> =0.23 XAn=0.15-0.22	XMg=0.16-0.14	
		XMg=0.41-0.47 Ti=0.10-0.24				

**Table 2 (continued). Mineral compositions for the studied metapelites**

	<b>Grt</b>	<b>Bt</b>	<b>Wm</b>	<b>Pl</b>	<b>St</b>	<b>Chl</b>	
<b>L-GHS</b>	<b>14-44a</b>		→	→			
		XMg=0.16-0.18	XMg <sup>i</sup> =0.57-0.60	Si=3.16-3.07	XAn=0.18-0.26		XMg*=0.48
		XCa=0.04-0.05	Ti <sup>i</sup> =0.11-0.15	Na=0.09-0.12			
		XMn=0.05-0.06	XMg=0.45-0.49	Si*=3.07-3.12			
		XFe=0.72-0.75	Ti=0.16-0.19	Na*=0.10			
	<b>14-61b</b>				→		
		XMg=0.12-0.13	XMg <sup>i</sup> =0.26-0.29	Si <sup>i</sup> =3.11-3.15	XAn <sup>i</sup> =0.11-0.12		
		XCa=0.02-0.03	Ti <sup>i</sup> =0.11-0.16	Na <sup>i</sup> =0.05-0.06	XAn=0.02-0.10		
XMn=0.03-0.04		XMg=0.28-0.34	Si=3.07-3.11				
	XFe=0.80-0.84	Ti=0.11-0.21	Na=0.05-0.09				
<b>14-71</b>				→			
	XMg=0.10-0.11	XMg <sup>i</sup> =0.35-0.42	Si=3.06-3.10	XAn <sup>i</sup> =0.18-0.20			
	XCa=0.04-0.03	Ti <sup>i</sup> =0.22-0.23	Na=0.12-0.14	XAn=0.14			
	XMn=0.035-0.040	XMg=0.28-0.36					
	XFe=0.84-0.87	Ti=0.15-0.25					
<b>14-52</b>				→			
	XMg=0.20-0.21	XMg <sup>i</sup> =0.50 Ti=0.12	Si <sup>i</sup> =3.08 Na <sup>i</sup> =0.045	XAn=0.12-0.15			
	XCa=0.025-0.03						
	XMn=0.11-0.12	XMg=0.47-0.55					
	XFe=0.64-0.67	Ti=0.14-0.23					
<b>U-GHS</b>	<b>14-08a</b>			→			
		XMg=0.10-0.12	XMg <sup>i</sup> =0.37-0.38	Si*=3.07-3.10	XAn <sup>i</sup> =0.33		XMg*=0.19
		XCa=0.035-0.045	Ti <sup>i</sup> =0.17	Na*=0.05-0.10	XAn=0.26-0.03		
		XMn=0.07-0.08	XMg=0.29-0.33				
		XFe=0.78-0.81	Ti=0.23-0.30				
	<b>14-12</b>				→		
XMg=0.10-0.11		XMg <sup>i</sup> =0.35-0.40	Si*=3.07-3.09	XAn <sup>i</sup> =0.20-0.21			
XCa=0.02		Ti <sup>i</sup> =0.04-0.09	Na*=0.06-0.09	XAn=0.22-0.02			
XMn=0.04-0.07		XMg=0.35-0.40					
	XFe=0.80-0.84	Ti=0.06-0.20					

The arrows indicate a zonation from core to rim; Ti, Si, Na are expressed as a.p.f.u.

<sup>i</sup> included in garnet. \* overgrowing Sm. <sup>f</sup> fibrolitic, replacing Grt and Wm at the rims <sup>#</sup> defining S<sub>m-1</sub>

Table 3 - Average pressure-temperatures estimates for the selected metapelites

	Sample	Assemblage	$a_{H_2O}$	T (°C)	P (kbar)	N° of reactions
<b>LHS</b>	15-19*	Grt-Bt-Wm-Pl-Qz-H <sub>2</sub> O	1	538±31	7.0±1.3	5
	15-19	Grt-Bt-Wm-Pl-Qz-H <sub>2</sub> O	1	591±23	7.5±1.0	5
	14-27a*	Grt-Bt-Wm-Pl-Qz-H <sub>2</sub> O	1	541±23	6.6±0.9	4
	14-27a	Grt-Bt-Wm-Pl-Qz-H <sub>2</sub> O	1	603±28	8.2±1.4	5
	15-28b	Grt-Bt-Wm-St-Ky-Qz-H <sub>2</sub> O	1	604±23	7.1±2.1	5
<b>LHS (RTS)</b>	15-26b*	Grt-Bt-Wm-Pl-Qz-H <sub>2</sub> O	1	584±25	7.8±1.0	4
	15-26b	Grt-Bt-Wm-Pl-Qz-H <sub>2</sub> O	1	607±24	8.8±1.0	4
<b>L-GHS</b>	14-03*	Grt-Bt-Wm-Pl-Qz-H <sub>2</sub> O	1	632±22	7.0±1.0	5
	14-03	Grt-Bt-Wm-Pl-Qz-H <sub>2</sub> O	1	673±31	8.7±1.3	5
			0.9	663±32	8.6±1.3	5
	14-25b*	Grt-Bt-Wm-Pl-Qz-H <sub>2</sub> O	1	602±25	6.4±1.2	4
	14-25b	Grt-Bt-Wm-Pl-Ky-Qz-H <sub>2</sub> O	1	660±37	8.3±2.1	6
			0.9	648±36	8.2±2.1	6
	15-38*	Grt-Bt-Wm-Pl-Qz-H <sub>2</sub> O	1	640±20	7.2±0.7	7
	15-38	Grt-Bt-Wm-Pl-St-Ky-Qz-H <sub>2</sub> O	1	678±17	8.7±1.0	9
			0.9	666±17	8.5±1.1	9
	14-24	Grt-Bt-Wm-Pl-Ky-Qz-H <sub>2</sub> O	1	711±35	8.9±1.9	6
			0.9	699±34	8.8±1.9	6
	14-44a	Grt-Bt-Wm-Pl-Ky-Qz-H <sub>2</sub> O	1	696±39	9.3±2.2	6
			0.9	676±34	8.9±1.9	6
	14-61b	Grt-Bt-Wm-Pl-Qz-H <sub>2</sub> O	0.9	701±42	9.8±1.7	6
	14-71	Grt-Bt-Wm-Pl-Qz-H <sub>2</sub> O	1	676±39	9.1±1.6	5
			0.9	662±55	8.3±2.3	5
14-52	Grt-Bt-Wm-Pl-Ky-Qz-H <sub>2</sub> O	1	850±68	11.3±2.6	7	
		0.9	835±67	11.3±2.7	7	
<b>U-GHS</b>	14-08a	Grt-Bt-Pl-Kfs-Sil-Qz-H <sub>2</sub> O	0.7	816±86	5.9±2.0	4
	14-12	Grt-Bt-Pl-Kfs-Sil-Qz-H <sub>2</sub> O	0.7	803±68	6.1±2.1	4

\* refer to the prograde mineral assemblage

Table 4

Table 4a - Summary of the peak P-T constraints obtained from pseudosections (with errors) and T/P ratios

		Sample	average T (°C)	error ( $\sigma$ ) T (°C)	weight T	average P (kbar)	error ( $\sigma$ ) P (kbar)	weight P	average T/P (°C/kbar)	error ( $\sigma$ ) T/P (°C/kbar)	weight T/P
Langtang- Gatlang	U-GHS	14-08	<b>780</b>	<b>20</b>		<b>7.8</b>	<b>0.8</b>		<b>101</b>	<b>12</b>	
		14-24	743	18	0.003	10.3	0.6	3.31	72	6	0.0320
	L-GHS	14-25b	720	5	0.040	9.9	0.2	44.44	73	1.6	0.3807
		14-03	720	10	0.010	10.3	0.7	2.04	70	6	0.0305
Gosainkund- Helambu	L-GHS	14-52	740	20	0.003	9.5	0.5	4.00	78	6	0.0260
		14-71	730	20	0.003	9.7	1.2	0.76	76	11	0.0081
		14-61b	740	10	0.010	10.4	1.0	1.11	71	8	0.0176
		14-44a	725	25	0.002	9.3	0.7	2.04	78	9	0.0137
		<i>weighted mean*</i>	<b>725</b>	<b>4</b>		<b>9.9</b>	<b>0.1</b>		<b>73</b>	<b>1.4</b>	
	LHS-RTS	15-26b	<b>635</b>	<b>15</b>		<b>9.6</b>	<b>0.9</b>		<b>66</b>	<b>7</b>	
	LHS	14-27a	<b>595</b>	<b>25</b>		<b>7.5</b>	<b>0.8</b>		<b>80</b>	<b>11</b>	

Table 4b - Summary of the peak P-T constraints obtained from "Average PT" method (with errors) and T/P ratios

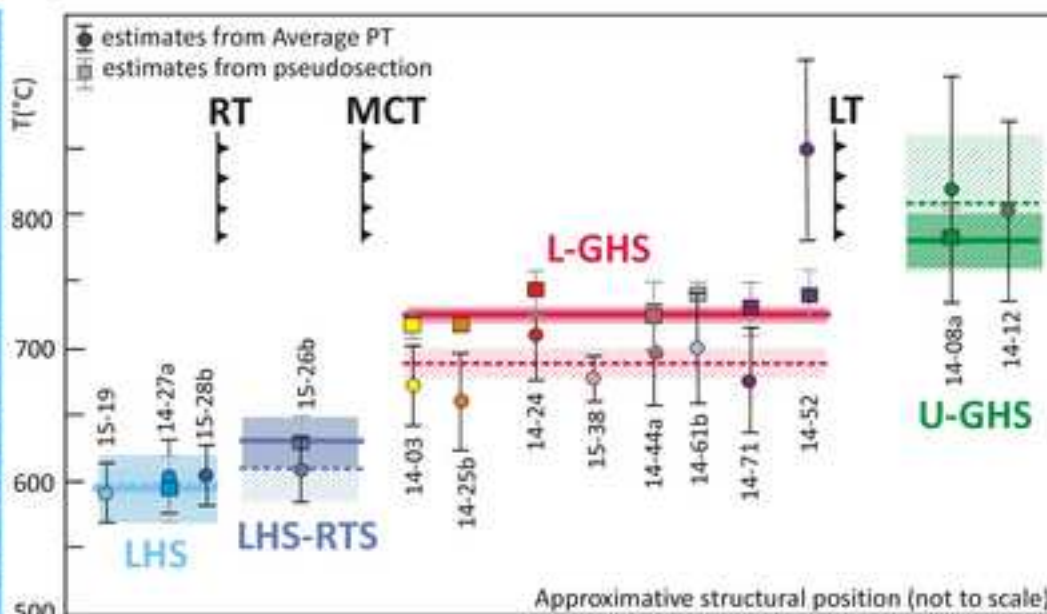
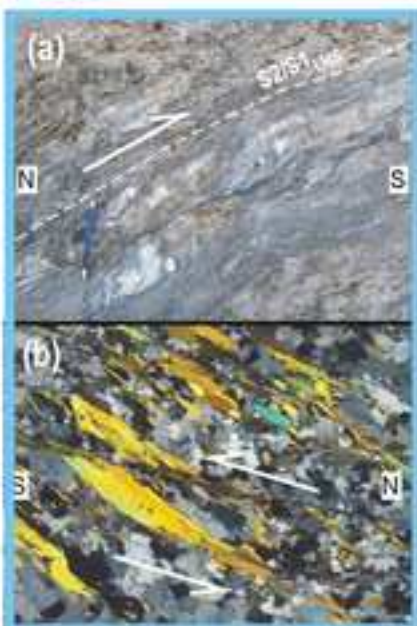
Langtang-Gatlang	U-GHS	14-12	803	68	0.0002	6.1	2.1	0.23	132	56	0.0003
		14-08a	816	86	0.0001	6.0	2.0	0.25	136	60	0.0003
		<i>weighted mean*</i>	<b>808</b>	<b>53</b>		<b>6.0</b>	<b>1.4</b>		<b>134</b>	<b>41</b>	
	L-GHS	14-24	711	35	0.0008	8.9	1.9	0.28	80	21	0.0023
		14-25b	660	37	0.0007	8.3	2.1	0.23	80	25	0.0017
15-38		678	17	0.0035	8.7	1.0	1.00	78	11	0.0084	
		14-03	673	31	0.0010	8.7	1.3	0.59	77	15	0.0044
Gosainkund- Helambu	L-GHS	14-52	850	68	0.0002	11.3	2.6	0.15	75	23	0.0018
		14-71	676	39	0.0007	9.1	1.6	0.39	74	17	0.0033
		14-61b	701	42	0.0006	9.8	1.7	0.35	72	17	0.0036
		14-44a	696	39	0.0007	9.3	2.2	0.21	75	22	0.0021
		<i>weighted mean*</i>	<b>687</b>	<b>11</b>		<b>9.0</b>	<b>0.6</b>		<b>76</b>	<b>6</b>	
	LHS-RTS	15-26b	<b>607</b>	<b>24</b>		<b>8.8</b>	<b>1.0</b>		<b>69</b>	<b>11</b>	
	LHS	15-28b	604	23	0.0019	7.1	2.1	0.23	85	28	0.0012
		14-27a	596	24	0.0017	7.5	0.9	1.23	79	13	0.0062
		15-19	591	23	0.0019	7.5	1.0	1.00	79	14	0.0054
		<i>weighted mean*</i>	<b>597</b>	<b>13</b>		<b>7.5</b>	<b>0.6</b>		<b>80</b>	<b>9</b>	

\*Where more than one sample are available, the weighted mean (with error) is calculated (i.e. values with smaller errors weight more than values with bigger errors).

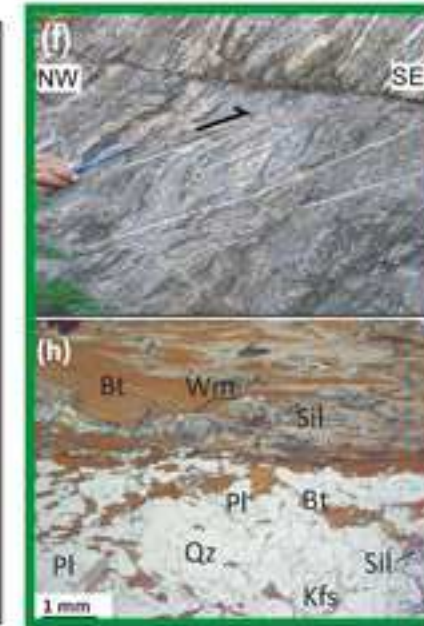
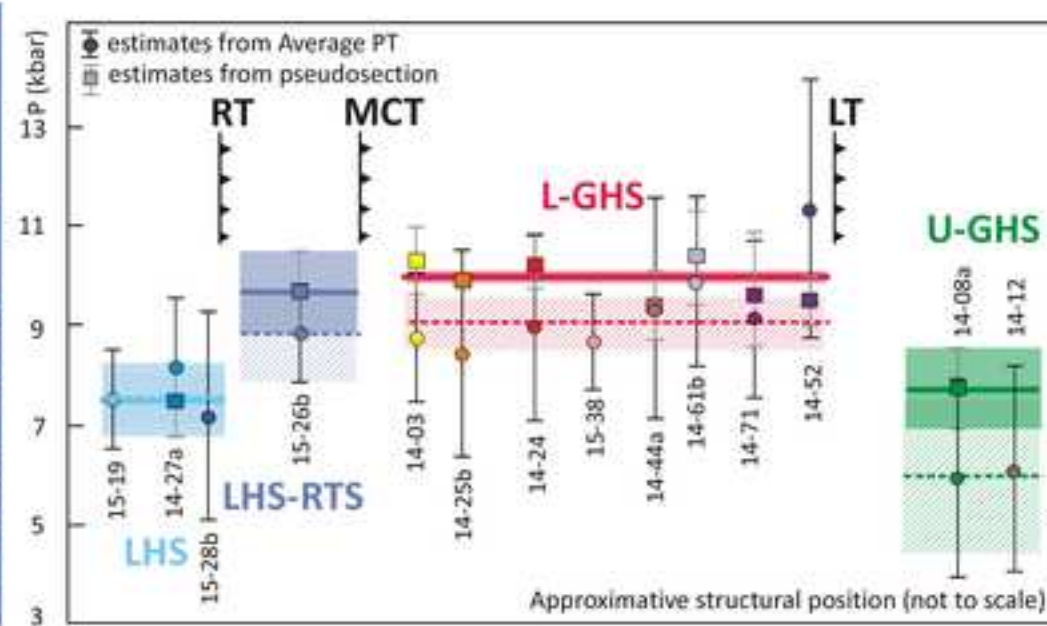
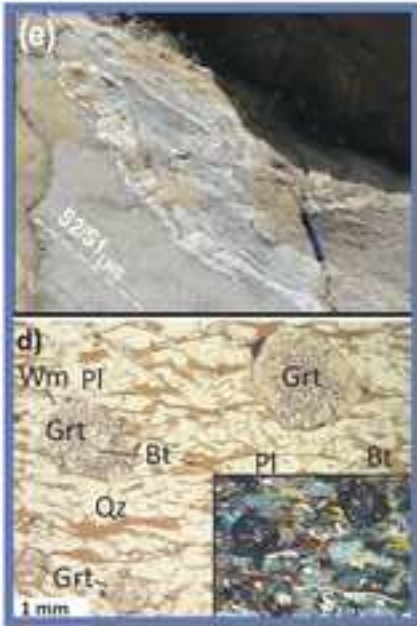
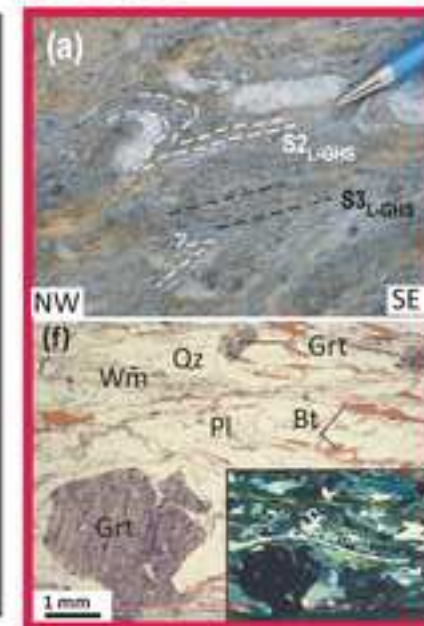
**Supplementary Material**

[Click here to download Supplementary Interactive Plot Data \(CSV\): Supplementary Material.docx](#)

## LHS



## L-GHS



## LHS-RTS

## U-GHS